Lunar Seismology: A Data and Instrumentation Review

Ceri Nunn[1,2] · Raphael F. Garcia[3] · Yosio Nakamura[4] · Angela G. Marusiak[5] ·
Taichi Kawamura[6] · Daoyuan Sun[7,8] · Ludovic Margerin[9] · Renee Weber[10] ·
Mélanie Drilleau[11] · Mark A. Wieczorek[12] · Amir Khan[13,14] · Attilio Rivoldini[15] ·
Philippe Lognonné[16] · Peimin Zhu[17]

Abstract Several seismic experiments were deployed on the Moon by the astronauts during the Apollo missions. The experiments began in 1969 with Apollo 11, and continued with Apollo 12, 14, 15, 16 and 17. Instruments at Apollo 12, 14, 15, 16 and 17 remained operational until the final transmission in 1977. These remarkable experiments provide a valuable resource. Now is a good time to review this resource, since the InSight mission is returning seismic data from Mars, and seismic missions to the Moon and Europa are in development from different space agencies. We present an overview of the seismic data available from

🖄 Springer

four sets of experiments on the Moon: the Passive Seismic Experiments, the Active Seismic Experiments, the Lunar Seismic Profiling Experiment and the Lunar Surface Gravimeter. For each of these, we outline the instrumentation and the data availability.

We show examples of the different types of moonquakes, which are: artificial impacts, meteoroid strikes, shallow quakes (less than 200 km depth) and deep quakes (around 900 km depth). Deep quakes often occur in tight spatial clusters, and their seismic signals can therefore be stacked to improve the signal-to-noise ratio. We provide stacked deep moonquake signals from three independent sources in miniSEED format. We provide an arrival-time catalog compiled from six independent sources, as well as estimates of event time and location where available. We show statistics on the consistency between arrival-time picks from different operators. Moonquakes have a characteristic shape, where the energy rises slowly to a maximum, followed by an even longer decay time. We include a table of the times of arrival of the maximum energy $t_{\max}$ and the coda quality factor Q_c.

Finally, we outline minimum requirements for future lunar missions to the Moon. These requirements are particularly relevant to future missions which intend to share data with other agencies, and set out a path for an International Lunar Network, which can provide simultaneous multi-station observations on the Moon.

1 Introduction

Many seismic experiments were deployed on the Moon by the astronauts during the Apollo missions. These experiments were part of the Apollo Lunar Seismic Experiments Package (ALSEP). The experiments began in 1969 with Apollo 11, and continued with Apollo 12, 14, 15, 16 and 17 (Fig. 1; Table 1). The seismic instruments included passive seismometers, a gravimeter, and geophones which were deployed in active source experiments, and then later in passive listening mode. Figure 2 shows the operating periods for each experiment. The passive seismic stations from Apollo 12, 14, 15 and 16 remained operational until the final transmission in 1977.

These remarkable experiments provide a valuable resource. Now is a good time to review this resource, since there is renewed scientific interest in planetary seismology. The Mars In-Sight mission carries a broadband seismometer and a short-period seismometer, which are detecting marsquakes on the surface of Mars (Lognonné et al. 2019; Banerdt et al. 2020; Giardini et al. 2020; Lognonné et al. 2020). The Seismometer to Investigate Ice and Ocean Structure (SIIOS) project is currently being tested in sites which are analogs for the icy moon Europa (e.g Marusiak et al. 2018; DellaGiustina et al. 2019; Marusiak et al. 2020).

[12]   Observatoire de la Côte d'Azur, CNRS, Laboratoire Lagrange, Université Côte d'Azur, Nica, France
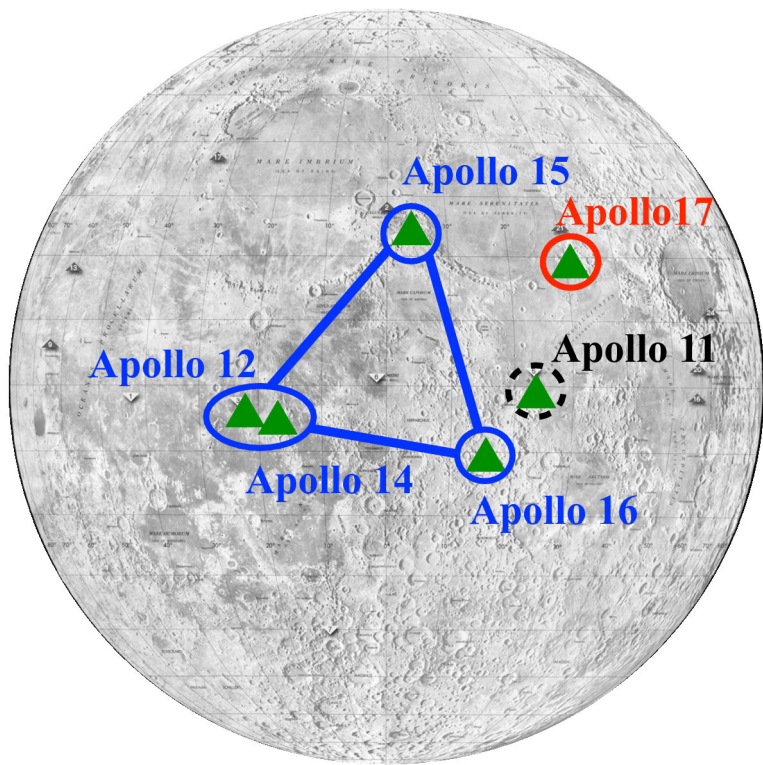
[13]   Institute of Theoretical Physics, University of Zurich, Zurich, Switzerland

[14]   Institute of Geophysics, ETH Zurich, Zurich, Switzerland

[15]   Observatoire Royal de Belgique, 3 Avenue Circulaire, 1050 Bruxelles, Belgium

[16]   Institut de Physique du Globe de Paris, CNRS, Université de Paris, Paris, 75005, France

[17]   China University of Geosciences, Wuhan, China

Fig. 1 Locations of the Apollo stations on the Moon. Passive Seismic Experiments (PSE) were based at Apollo 11, 12, 14, 15 and 16 (station 11 was only operational for one lunation). Active Seismic Experiments (ASE) were based at Stations 14 and 16. A second active experiment, known as the Lunar Seismic Profiling Experiment (LSPE) was based at station 17. Station 17 also included the Lunar Surface Gravimeter (LSG), which is a source of additional passive seismic information

Table 1 Locations of the Apollo seismic stations. Coordinates given are for the Passive Seismic Experiments (PSE) and for the Apollo Lunar Surface Experiment Package (ALSEP), which includes the active experiments. Coordinates are given in the DE421 mean Earth/rotation axis reference frame (Williams et al. 2008). From Table 5 in Wagner et al. (2017)

Station	Coordinates	
	Latitude	Longitude
A11 PSE	0.67322	23.47315
A12 PSE	−3.0099	336.5752
A14 PSE	−3.64408	342.52233
A14 ALSEP	−3.64419	342.52232
A15 PSE	26.13411	3.62980
A15 ALSEP	26.13406	3.62991
A16 PSE	−8.9759	15.4986
A16 ALSEP	−8.9759	15.4986
A17 ALSEP	20.1923	30.7655

Efforts in many countries indicate that an International Lunar Network of seismic stations could be deployed on the Moon by the mid-2020s. In China, CNSA's Chinese Lunar Exploration Program deployed a lunar rover with the Chang'e 3 and Chang'e 4 missions. China is
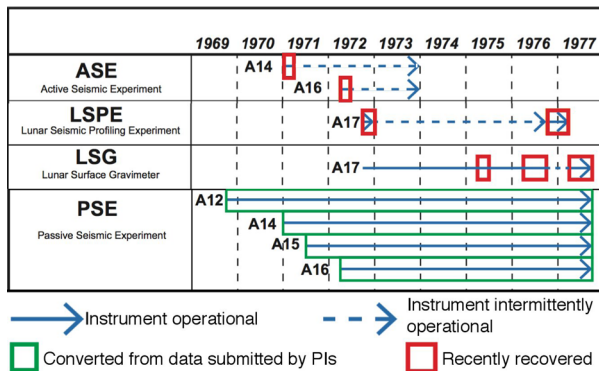
Fig. 2 Overview of the operating periods of the Apollo seismic experiments, and data availability. Solid blue lines indicate mainly operational instruments (with just occasional outages and data loss). Dashed lines indicate instruments which were mostly on standby but were occasionally turned on in their listening mode. Additional passive seismic data are available from Apollo 11 from 21 July to 3 August 1969 and again from 19 to 26 August 1969. After Nagihara et al. (2017)

planning Chang'e 5 and 6 as sample return missions (Goh 2018). In the USA, a Lunar Geophysical Network is one of the possible candidates for the NASA New Frontiers 5 mission (National Research Council 2011; Shearer and Tahu 2011). The network would deploy at least three stations containing geophysical instruments, and potentially cover the farside of the Moon (Yamada et al. 2011; Mimoun et al. 2012). In Japan, JAXA's SLIM (Smart Lander for Investigating the Moon) is currently under development (JAXA 2018). Dragonfly is a Titan mission which uses a rotorcraft-lander. It has been selected as NASA's next New Frontiers mission (APL 2019). There is considerable interest in using seismology to explore the icy moons within our solar system (Vance et al. 2018). Lognonné and Johnson (2015) contains a review of past and future planetary seismology.

It is important that the data from the Apollo experiments can continue to be used in the future. Recent efforts have been made to preserve and document as much of the data as possible, since some of the data remain on digital tapes which are deteriorating in quality. Some tapes may have been permanently lost. The original data from the Apollo experiments were sent to the Principal Investigator (PI) for each experiment. The PIs were responsible for checking the data, and then archiving them. In some cases, especially where problems were discovered with the data, the data were not archived. Some of these data have recently been recovered (Nagihara et al. 2017). Dimech et al. (2017) analyzed thermal moonquakes with recently rediscovered data from Apollo 17. Similarly, Nagihara et al. (2018) recovered 10% of the data missing from a heat flow experiment which ran from 1974 to 1977.

The authors of this paper are members of an international team sponsored by the International Space Science Institute in Bern and in Beijing. The team formed to gather a set of reference data sets and internal structural models of the Moon. This paper reviews the available data, and the companion paper (Garcia et al. 2019) reviews lunar structural models. Within this paper, we also outline minimum requirements for a future International Lunar Network (ILN). If funded, NASA would provide two or more nodes, and other nations would provide additional nodes (National Research Council 2011). These requirements are particularly relevant to future missions which intend to share data with other agencies, and set out a path for simultaneous multi-station observations on the Moon.

2 Apollo Seismic Instruments

More than 40 years after the termination of the experiments, the Apollo data continue to provide important insights for lunar seismology. The Apollo Lunar Surface Experiment Packages (ALSEPs) were a unique series of in-situ geophysical experiments, which included seismic experiments. No seismic observations have been performed on the Moon since Apollo. The experiments included the Passive Seismic Experiment (PSE), the Active Seismic Experiment (ASE), and the Lunar Surface Profiling Experiment (LSPE). For decades, these data have been used to investigate the internal structure of the Moon (e.g. Nakamura 1983; Lognonné et al. 2003; Weber et al. 2011; Garcia et al. 2011). In addition to these experiments, the Lunar Surface Gravimeter (LSG) also provides some seismic information (Kawamura et al. 2015). In this section, we review the instrumentation.

2.1 Passive Seismic Experiments (PSE)

The Passive Seismic Experiments (PSE) were performed at Apollo 11, 12, 14, 15, and 16. Figure 2 shows the observation period of each station. Apollo 11 functioned for only about 3 weeks. Stations 12, 14, 15 and 16 operated continuously since their deployment and functioned as a seismic network until September 1977, when all the remaining experiments were shut down. More than 13000 seismic events were cataloged using data from the mid-period instruments during the operation of the network (Nakamura et al. 1981). The four stations formed an almost equilateral triangle, with stations 12 and 14 at one corner (Fig. 1). The network covered only a portion of the lunar nearside. This is likely one of the reasons that most of the detected seismic events are from the lunar nearside. Each PSE station was equipped with a 3-component (two horizontal and one vertical) mid-period displacement sensors and a vertical-component short-period (SP). Earlier papers referred to the mid-period seismometer as long-period. We use the designation mid-period to be consistent with the IRIS naming conventions, and to better describe the capabilities of the seismometer.

The mid-period (MP) sensors were feedback displacement transducers (Sutton and Latham 1964), with a single-pole high-pass output level stabilizer, and an 8-pole low-pass output anti-aliasing filter for each. The SP sensor was a standard coil-magnet velocity transducer, also with a single-pole high-pass output level stabilizer and an 8-pole low-pass output anti-aliasing filter. The feedback signals from the MP sensors were recorded as tidal (TD) signal outputs.

The MP sensor had two modes for seismic observation. These were the peaked mode and the flat mode. The peaked mode was the natural response of the seismometer, and the seismometer did not include a feedback filter. The flat mode was designed to be sensitive to a broader range of frequencies, and used a feedback filter in the circuit. Unfortunately, the flat mode was not very stable. Therefore, the seismometers were mainly operated in peaked mode. All of these outputs went through pre- and post-amplifiers before they were fed to the input of the analog-to-digital converter for digitization. Table 2 summarizes the periods when the MP seismometer was functioning in flat mode.

Figure 3 shows the transfer function for the short-period (SP) and mid-period (MP) sensors. The SP sensor has a displacement response peaked at approximately 8 Hz, as the sensitivity of the instrument falls off above this frequency (see Fig. 3). The peaked mode of the MP sensor has a peak at about 0.45 Hz while the flat mode has flat response (for displacement) from about 0.1 to 1 Hz.

Although the two horizontal components for the MP sensor were intended to point north and east, they were misaligned for stations S12 and S16. Section S1 in the electronic supplement contains the correct orientations. We provide only the nominal sampling rates for
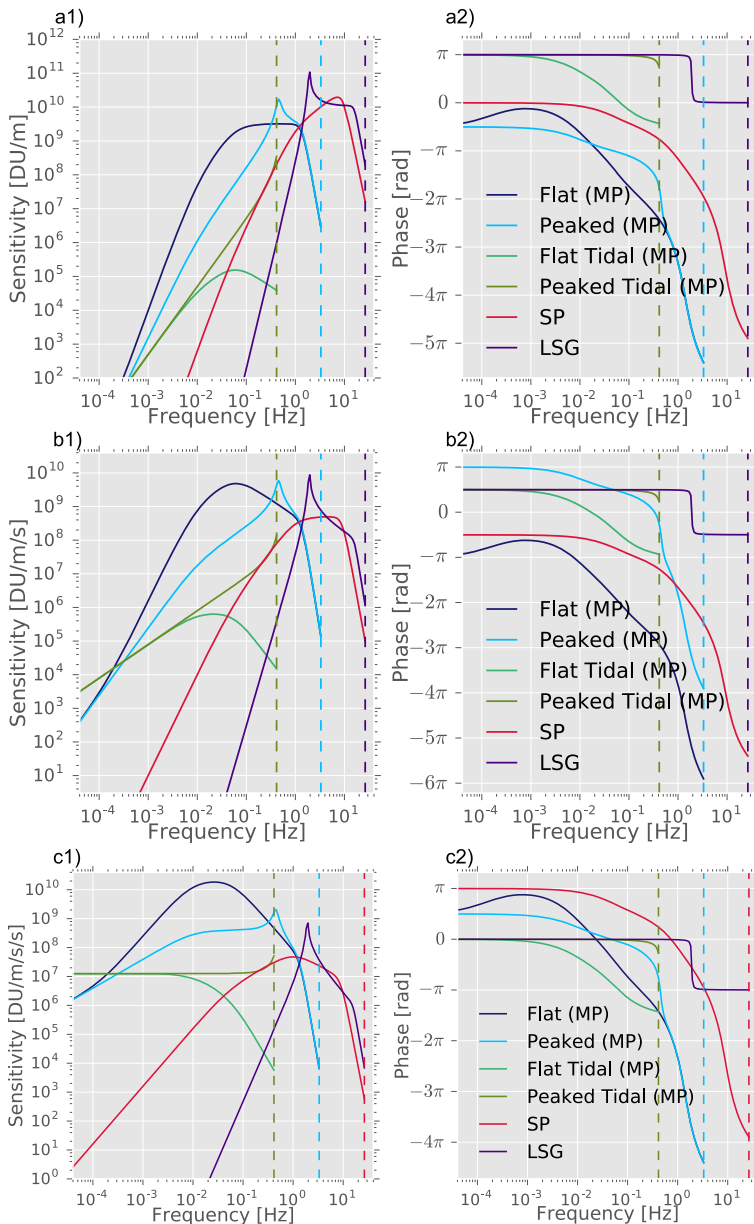
Fig. 3 Amplitude (left) and phase (right) transfer functions for the flat and peaked modes and tidal outputs of the mid-period seismometer, the short-period (SP) and the lunar surface gravimeter (LSG). The amplitude of the transfer function is shown in displacement (**a1**), velocity (**b1**) and acceleration (**c1**). DU stands for digital units. The units are DU/m, DU/(m/s) and DU/(m/s^2), respectively. The phase response is shown in displacement (**a2**), velocity (**b2**), and acceleration (**c2**). The plots show the nominal responses up to the Nyquist frequency (dashed lines). The phases show the counterclockwise angle from the positive real axis on the complex plane in radians

Table 2 Flat Mode Operation: The main times when the mid-period seismometers were operating in flat mode. For the remainder of the time they operated in peaked mode. Note that the seismometers were frequently changed from peaked mode to flat mode and back again during tests

Station	Flat mode operation
S12	1974-10-16T14:02:36.073–1975-04-09T15:31:03.702
	1975-06-28T13:48:23.124–1977-03-27T15:41:06.247
S14	1976-09-18T08:24:35.026–1976-11-17T15:34:34.524
S15	1971-10-24T20:58:47.248–1971-11-08T00:34:39.747
	1975-06-28T14:36:33.034–1977-03-27T15:24:05.361
S16	1972-05-13T14:08:03.157–1972-05-14T14:47:08.185
	1975-06-29T02:46:45.610–1977-03-26T14:52:05.483

all the seismometers. Small variations in the actual sampling rates were observed at all sites (Nunn et al. (2017) and Knapmeyer-Endrun and Hammer (2015, Supplement)). This was particularly due to the large temperature variations on the surface of the Moon. The data were time-stamped when the signal was received on Earth. When an accurate time-signal was unavailable the timing was estimated using the so-called 'software clock'. Nakamura (2011) found errors of up to one minute between the software clock and the real time, and showed how these errors affected some travel-time estimates.

Until February 29, 1976, the scientific data from Apollo were processed and compiled at NASA's Johnson Space Center, and delivered to the principal investigator for each scientific experiment, and later submitted to the National Space Science Data Center for archiving. Depending on the experiment, data were submitted in either their original or processed form. By mid-1975, the analysis contracts with most of the individual principal investigators were terminated (Bates et al. 1979). However, the instruments continued to generate and return observational data. To decrease costs, the data processing was transferred to the University of Texas at Galveston. The transfer was completed in March 1976 and the data were sent to the University of Texas until the experiments were terminated in September 30, 1977.

2.1.1 Flat-Response Mode of the Mid-Period Seismometer

In flat-response mode, the seismometer response $A_{MPF}(\omega)$ for acceleration is represented by:

$$A_{MPF}(\omega) = K_3 F_a(\omega) F_l(\omega) F_{sf}(\omega) \quad \frac{V}{(m/s^2)} \tag{1}$$

where ω is the angular frequency, and K_3 is the amplifier gain of the feedback output.

$F_a(\omega)$ is the transfer function of the single-pole high-pass filter in the output amplifier,

$$F_a(\omega) = \frac{s(\omega)}{\omega_a + s(\omega)} \tag{2}$$

$$s(\omega) = j\omega \tag{3}$$

where ω_a is the output high pass cut-off angular frequency, and $j^2 = -1$.

$F_l(\omega)$ is the transfer function of the 8-pole output low-pass anti-aliasing filter,

$$F_l(\omega) = \left[\frac{\omega_l^2}{s(\omega)^2 + 2\cos\left(\frac{\pi}{8}\right)\omega_l s(\omega) + \omega_l^2} \right]^2 \left[\frac{\omega_l^2}{s(\omega)^2 + 2\cos\left(\frac{3\pi}{8}\right)\omega_l s(\omega) + \omega_l^2} \right]^2 \tag{4}$$

where ω_l is the output low-pass cut-off angular frequency and $\omega_l = 2\pi f_l$.

$F_{sf}(\omega)$ is the transfer function of the feedback component of the seismometer,

$$F_{sf}(\omega) = \frac{K_1 S(\omega) F_d(\omega)}{1 + K_1 K_2 S(\omega) F_d(\omega) F_f(\omega)} \tag{5}$$

K_1 is the gain of the displacement transducer in V/m, and K_2 is the coil-magnet transfer function in (m/s^2)/V.

$F_d(\omega)$ is the transfer function of the demodulator low-pass filter,

$$F_d(\omega) = \frac{\omega_d}{s(\omega) + \omega_d} \tag{6}$$

where ω_d is the demodulator low-pass cut-off angular frequency.

$S(\omega)$ is the transfer function of the seismometer for acceleration:

$$S(\omega) = \frac{1}{s(\omega)^2 + 2h\omega_0 s(\omega) + \omega_0{}^2}$$
$$\omega_0 = 2\pi f_0 \tag{7}$$

where f_0 is the resonant frequency of the pendulum and h is the damping constant.

$F_f(\omega)$ is the transfer function of the feedback low-pass filter,

$$F_f(\omega) = \frac{\omega_f}{s(\omega) + \omega_f} \tag{8}$$

where ω_f is the feedback low-pass cut-off angular frequency. The parameters for the mid-period seismometer have the following values (Yamada 2012):

$$K_1 = 500000 \text{ V/m}$$

$$K_2 = 0.000016 \ \frac{\text{m/s}^2}{\text{V}}$$

$$K_3 = 31.6$$

$$\omega_a = 0.0628 \text{ rad/s}$$

$$\omega_l = 8.72665 \text{ rad/s}$$

$$f_0 = 0.06667 \text{ Hz}$$

$$h = 0.85$$

$$\omega_d = 47.62 \text{ rad/s}$$

$$\omega_f = 0.000997 \text{ rad/s}$$

$$\text{Sampling Rate} = 6.625 \text{ Hz (nominal)}$$

To convert the seismometer response to velocity in V/(m/s), we multiply $A_{MPF}(\omega)$ by the function $s(\omega)$. To convert it to displacement in V/m, we multiply it by the square of $s(\omega)$, as follows:

$$V_{MPF}(\omega) = s(\omega) A_{MPF}(\omega) \quad \text{V/(m/s)} \tag{9}$$

$$D_{MPF}(\omega) = s(\omega)^2 A_{MPF}(\omega) \quad \text{V/m} \tag{10}$$

The instrument output voltages between -2.5 V and $+2.5$ V and the digitizer recorded digital units between 0 and 1023. Therefore, we can convert the transfer function from V/m to DU/m by multiplying by 1024 DU/5 V, which is the reciprocal value of the 1-LSB (least significant bit) of the analog-to-digital converter:

$$K = 204.8 \text{ DU/V} \tag{11}$$

The transfer function in flat mode is shown in Fig. 3.

2.1.2 Peaked-Response Mode of the Mid-Period Seismometer

The seismometer response during peaked-response mode $A_{LPP}(\omega)$ is represented by eliminating the transfer function of the feedback low-pass filter $F_f(\omega)$ from the equation of $A_{LPP}(\omega)$:

$$A_{LPP}(\omega) = K_3 F_a(\omega) F_l(\omega) F_{sp}(\omega) \quad \frac{\text{V}}{(\text{m/s}^2)}$$

$$F_{sp}(\omega) = \frac{K_1 S(\omega) F_d(\omega)}{1 + K_1 K_2 S(\omega) F_d(\omega)} \tag{12}$$

The transfer function in peaked mode is shown in Fig. 3, and a block diagram which covers both the peaked and flat modes is included in the Electronic Supplement.

2.1.3 Tidal-Response of the Mid-Period Seismometer

The tidal output is the un-amplified feedback signal proportional to the mid-period boom motion (the feedback component of the seismometer $F_{sf}(\omega)$, followed by an additional low-pass feedback $F_f(\omega)$). This signal potentially gives changes to the gravity field and tidal acceleration, since it has higher sensitivity than the mid-period output at longer periods. It records only once every eight samples of the mid-period instrument, giving a nominal sampling rate of 0.828125 Hz. The flat tidal-mode response in acceleration is:

$$A_{TDF}(\omega) = F_{sf}(\omega) F_f(\omega) \quad \frac{\text{V}}{(\text{m/s}^2)} \tag{13}$$

or alternatively:

$$A_{TDF}(\omega) = \frac{K_1 S(\omega) F_d(\omega) F_f(\omega)}{1 + K_1 K_2 S(\omega) F_d(\omega) F_f(\omega)} \quad \frac{\text{V}}{(\text{m/s}^2)} \tag{14}$$

We noticed problems with earlier formulations of the tidal mode. Figure 4.2 in Teledyne (1968) (reproduced in the Electronic Supplement) does not include a second wire between the filter switch and the feedback resistor (R_{fb} in their diagram). We found a different problem in Fig. 3 in Yamada (2012), which was based on Fig. 2 in Horvath (1979). The tidal output should be connected to the peaked-mode output of the switch, and thus to the input of K_2. Instead it is connected to the input of the mode switch.

There is also a peaked mode of this signal, which is as follows:

$$A_{TDP}(\omega) = \frac{K_1 S(\omega) F_d(\omega)}{1 + K_1 K_2 S(\omega) F_d(\omega)} \quad \frac{\text{V}}{(\text{m/s}^2)} \tag{15}$$

For both the flat and peaked tidal modes, we multiply by the square of the function $s(\omega)$ to convert the response to displacement. Finally, the conversion K between volts and digital units (DU/V) is applied. Figure 3 shows the transfer function for the tidal mode.

2.1.4 Response of the Short-Period Seismometer

The transfer function of the short-period sensor $A_{SP}(\omega)$ in acceleration is expressed by

$$A_{SP}(\omega) = GG_1 G_2 S_p(\omega) F_a(\omega) F_l(\omega) \quad \frac{V}{(m/s^2)} \tag{16}$$

where G_1 is the generator constant of the magnet-coil system and G_2 is the pre-amplifier gain. G is the resistance ratio of the damping circuit, which is expressed by

$$G = \frac{R_s}{R_g + R_s} \tag{17}$$

where R_s is the damping resistance and R_g is the coil resistance in ohms. $S_p(\omega)$ is the transfer function of the short-period sensor in acceleration

$$S_p(\omega) = \frac{s(\omega)}{s(\omega)^2 + 2h\omega_0 s(\omega) + \omega_0^2} \tag{18}$$

where ω_0 is the resonant frequency in rad/s.

$F_a(\omega)$ is the transfer function of high-pass filter of the amplifier (Eq. (2)) and $F_l(\omega)$ is the transfer function of the low-pass anti-aliasing filter (Eq. (4)). Finally, the conversion K between volts and digital units (DU/V) is applied.

The parameters for the short-period seismometer have the following values:

$$R_g = 1800 \ \Omega$$

$$R_s = 2680 \ \Omega$$

$$G_1 = 175 \ \frac{V}{m/s}$$

$$G_2 = 23700$$

$$f_0 = 1 \ Hz$$

$$h = 0.85$$

$$\omega_b = 0.31416 \ rad/s$$

$$\omega_p = 57.1199 \ rad/s$$

$$K = 204.8 \ DU/V$$

Sampling Rate $= 53$ Hz (nominal)

The values are from Yamada (2012), (except K, which was derived in Sect. 2.1.1). The short-period transfer function is shown in Fig. 3, and a block diagram is included in the Electronic Supplement.
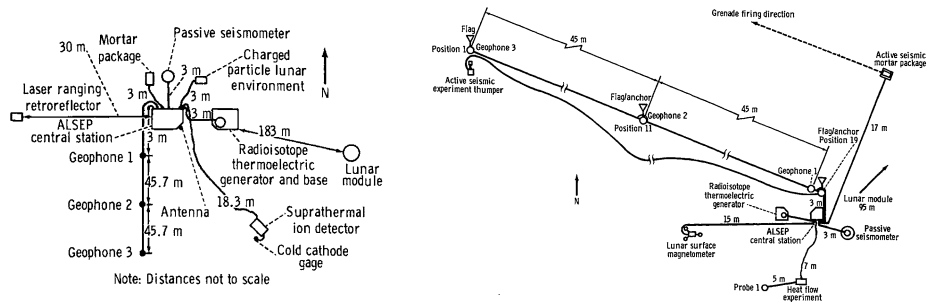
Fig. 4 Geometric configuration for the Apollo Active Seismic Experiment for station 14 (left) and station 16 (right). Reproduced from Figs. 1-3 and 1-5 from Bates et al. (1979)

2.2 Active Seismic Experiment (ASE)

Active seismic experiments were performed at stations 14 and 16 with a small array of geophones. In contrast to the passive experiments, which were primarily designed to detect natural seismic events, the active experiments were designed to evaluate the subsurface structure around the landing site using controlled seismic sources. For both stations, three geophones were deployed to form a linear array (Fig. 4). The nominal distance between the geophones was 45.7 m (Kovach et al. 1971). The geophones were labeled as geophone 1, 2 and 3, with geophone 1 closest to the Central Station. Two types of seismic sources were used for the exploration. The first was a thumper equipped with a small explosive. The thumper at station 14 had 21 initiators, all located next to a geophone. Successful shots were number 1 (at geophone 3); 2, 3, 4, 7 and 11 (at geophone 2); and 12, 13, 17, 18, 19, 20 and 21 (at geophone 3) (Kovach et al. 1971). At station 16, shot number 1 started at the location of geophone 3 and traversed towards geophone 1 with 4.75 m intervals (except for between shot 11 and 12 and shot 18 and 19, where the interval was set to 9.5 m) (Kovach et al. 1972).

The second seismic source used rocket-launched grenades which impacted at a location distant from the geophone array. The grenades were designed to probe different depths at the landing site. Unfortunately, the grenade experiment was not performed at station 14 due to the fear that the back-blast might damage the other instruments. Table 3 shows the launch details for station 16. The grenades reached approximate distances of 914 m, 305 m and 152 m from the array. Kovach et al. (1971) and Kovach et al. (1972) monitored several additional signals, including the thrust of the Apollo 14 and Apollo 16 Lunar Module ascent. They estimated the structure of the local subsurface using a combination of active and passive sources. Kovach et al. (1971, 1972) and Brzostowski and Brzostowski (2009) describe more details of the experiment.

The active seismic experiments (ASE) used geophones, which covered higher frequencies compared to the passive experiments. The transfer function $A_{ASE}(\omega)$ for acceleration is represented by:

$$A_{ASE}(\omega) = AGS_p(\omega) \quad \frac{V}{(m/s^2)} \tag{19}$$

where A is the amplifier gain, G is the generator constant and S_p is a transfer function for acceleration (Eq. (18)).

In addition, the experiment used an 8th-order low-pass filter (McAllister et al. 1969). The filter type is not specified. However, we find a reasonable fit to Fig. 7-5 of Kovach et al.

Table 3 Nominal Grenade Parameters for the Active Seismic Experiment at Apollo 16. Grenade 2 was launched first, followed by 4 and then 3. Grenade 1 was not launched, due to a problem with the pitch angle following the launch of grenade 3. The experiments were carried out on May, 23, 1972 from 05:20:00 to 06:44:00. The launch times were not known precisely. A method to estimate the traveltimes is given in Kovach et al. (1971). Parameters are from McDowell (1976). The original range measurements were specified in feet. Note that Kovach et al. (1971) converted these only very roughly to meters

Parameter	Grenade No.			
	1	2	3	4
Range (m)	1524	914	305	152
Mass (kg)	1.261	1.024	0.775	0.695
Mean velocity (m/s)	50	38	22	16
Lunar flight time (s)	44	32	19	13
Launch angle (deg)	45	45	45	45

(1971) with a Butterworth filter:

$$F_l(\omega) = \frac{1}{\sqrt{1 + \left(\frac{\omega}{\omega_l}\right)^{2n}}} \tag{20}$$

where n is the order of the filter, and ω_l is the cutoff angular frequency.

Table 4 and Table 5 summarize the parameters for station 14 and 16, respectively. We stress that we are quoting the nominal parameters. We also did not fit the low frequencies well, and suspect that there was a pre-amplifier. McAllister et al. (1969) describes how to calibrate the instrument responses.

The active seismic experiment (ASE) used logarithmic compression to prevent saturation and to use the full waveform. The input voltage V_{in} was compressed, to give a new output voltage V_{out}. This output voltage was digitized and given values from 0 to 31. Digital unit (DU) values from 0–13 represented negative input voltage, DU values from 17–31 represented positive inputs and DU values from 14–16 represented the linear portion without logarithmic compression.

The output voltage of the ASE signal was 5 V and the digital output was recorded in 5-bit integers. The following expression recovers the seismometer output voltage V_{out} from the digital output D_{out}:

$$V_{out} = \frac{D_{out} - D}{K_g} \tag{21}$$

We can recover the pre-compressed input voltage V_{in} using the following expression from Yamada (2012):

$$
\begin{aligned}
V_{in} &= -\exp\left[\frac{V_{out} - b_{neg}}{M_{neg}}\right] & \text{if } V_{out} < 2.170 \\
V_{in} &= \frac{V_{out} - 2.420}{M_1} & \text{if } 2.170 < V_{out} < 2.670 \\
V_{in} &= \exp\left[\frac{V_{out} - b_{pos}}{M_{pos}}\right] & \text{if } 2.670 < V_{out}
\end{aligned}
\tag{22}
$$

Table 4 Apollo 14 Active Seismic Experiment (ASE) Sensor Parameters. The resonant frequency, generator constant and amplifier gain are from Table 7.1 in Kovach et al. (1971). The low-pass filter order and cutoff are from McAllister et al. (1969). We estimated the damping constant by fitting it to Fig. 7-5 of Kovach et al. (1971). We calculated the values for the conversion coefficient K_g and the conversion constant D using Table 5-VI in Lauderdale and Eichelman (1974). Yamada (2012) estimated the logarithmic compression parameters (M_{neg}, M_{pos}, b_{neg}, b_{pos} and M_1) using calibration data provided by Y. Nakamura. The nominal sampling rate is from Table A1 in MSC (1971). We noticed that the sampling rate is sometimes incorrectly quoted as 500 Hz

| Parameter	Geophone No.		
	1	2	3
Resonant frequency (f_0 Hz)	7.32	7.22	7.58
Generator constant (G V/(m/s))	250.4	243.3	241.9
Damping constant (h)	0.45	0.45	0.45
Amplifier gain (A) (at 10 Hz and $V_{input} = 0.005$ V rms)	666.7	666.7	675.7
Cutoff (f_l Hz)	250		
Filter order (n)	8		
Conversion coefficient (K_g DU/V)	6.3500		
Conversion constant (D DU)	-0.3750		
M_{neg} for DU $= 0$–13	-0.26996	-0.26996	-0.27128
M_{pos} for DU $= 17$–31	0.27046	0.26984	0.27088
b_{neg} for DU $= 0$–13	0.29296	0.28192	0.27628
b_{pos} for DU $= 17$–31	4.55135	4.55342	4.55694
M_1	332	332	332
Nominal sampling rate (Hz)	530		

Table 4 and Table 5 include the parameters for station 14 and 16, respectively. One of the transfer functions for station 14 is shown in Fig. 5.

2.3 Lunar Seismic Profiling Experiment (LSPE)

Another active experiment was performed at station 17. The aim of Lunar Seismic Profiling Experiment (LSPE) was to explore the subsurface down to a few kilometers, which was much deeper than the previous active seismic experiments. A larger geophone array was established with four geophones (Fig. 6, top panel). Eight explosive packages, equipped with different amounts of high explosives, were used as the seismic source. The four geophones formed a triangular array with an additional geophone at the center of the triangle. The outer sensors were approximately 100 m apart. The geophones were miniature moving coil-magnet seismometers. All eight explosives were successfully deployed during the extravehicular activity (EVA), and detonated after the astronauts left the Moon (Fig. 6, lower panel). Table 6 shows the amount of explosives and the detonation time for each explosive package. The LSPE was also turned on to observe the impulse produced by the thrust of lunar module ascent engine. Geophone 1 was approximately 148 m west-northwest of the lunar module (Kovach et al. 1973). The LSPE also detected the impact of the lunar module, which impacted approximately 8.7 km away. Finally, the LSPE was also turned on from August 15, 1976 to April 25, 1977 for passive observation. Haase et al. (2013) improved on

Table 5 Apollo 16 Active Seismic Experiment (ASE) Sensor Parameters. The resonant frequency, generator constant, damping parameters and amplifier gain are from Table 10.1 in Kovach et al. (1972). Other parameters from the same sources as Table 4

Parameter	Geophone No.		
	1	2	3
Resonant frequency (f_0 Hz)	7.42	7.44	7.39
Generator constant (G V/(m/s))	255	255	257
Damping constant (h)	0.5	0.5	0.5
Amplifier gain (A) (at 10 Hz and $V_{input} = 0.275$ V peak to peak)	698	684	709
Cutoff (f_l Hz)	150		
Conversion coefficient (K_g DU/V)	6.3500		
Conversion constant (D DU)	−0.3750		
M_{neg} for DU = 0–13	−0.26858	−0.26983	−0.27054
M_{pos} for DU = 17–31	0.26773	0.27065	0.26813
b_{neg} for DU = 0–13	0.28260	0.30123	0.26124
b_{pos} for DU = 17–31	4.55780	4.55798	4.55303
M_1	332	332	332
Nominal sampling rate (Hz)	530		
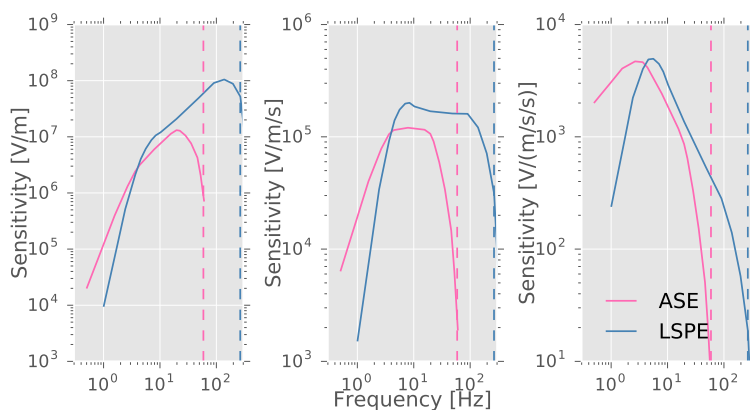
Fig. 5 Nominal transfer functions for the active seismic experiment (ASE, based on Fig. 7-5 in Kovach et al. (1971)) and the lunar seismic profiling experiment (LSPE, based on Fig. 10-4 in Kovach et al. (1973)). Displacement is shown in V/m, velocity in V/(m/s), and acceleration in V/(m/s^2)

the original approximate estimates of the coordinates for the dimensions of the geophone array and the locations of the explosives using images from Lunar Reconnaissance Orbiter. Heffels et al. (2017) used these coordinates to re-estimate the subsurface velocity structure. Kovach et al. (1973) and Brzostowski and Brzostowski (2009) contain further details about the experiment.

The Lunar Seismic Profiling Experiment (LSPE) used the same geophones as the Active Seismic Experiment (ASE). The logarithmic compression was similar to the active experi-
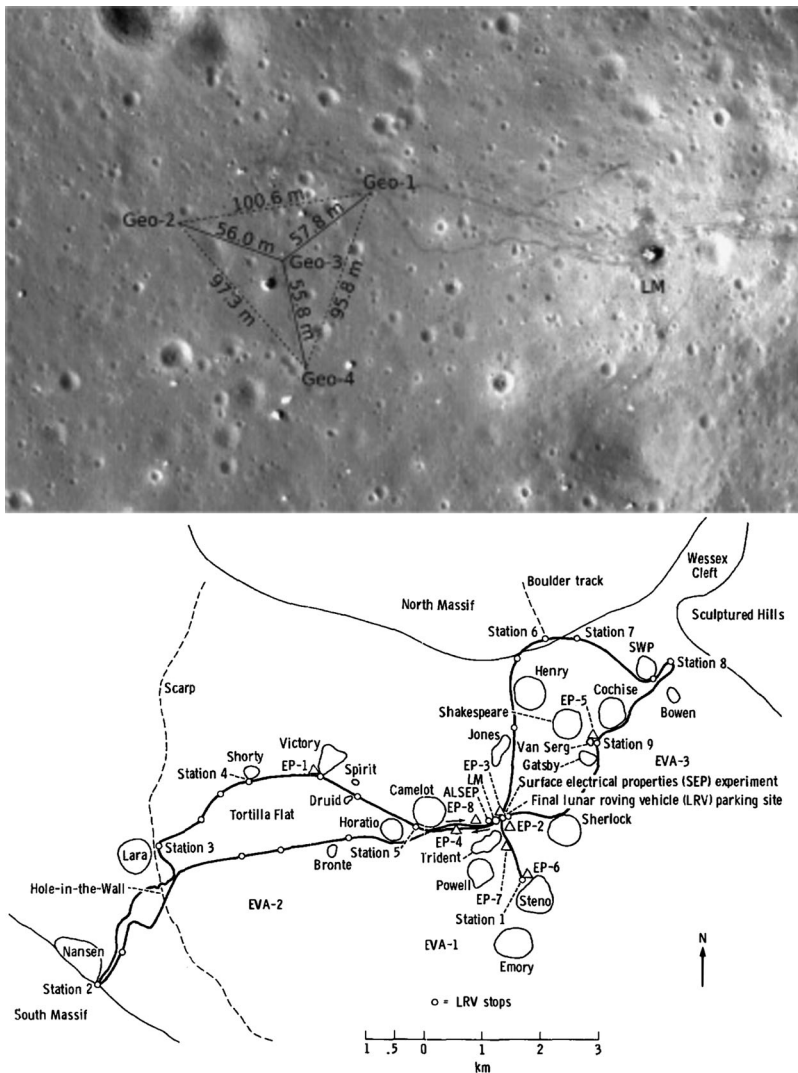
Fig. 6 Geometric configuration for the Apollo Lunar Seismic Profiling Experiment for Apollo 17. The top panel shows the geometry of the geophone array of the experiment (Heffels et al. 2017). The bottom panel shows the traverse of the extravehicular activity (EVA). 'EP' marks the positions of the explosives (Kovach et al. 1973)

ment. The digital output for the LSPE was from 0 to 123. Unlike the ASE, the LSPE had no linear section in the middle of the digitizer range. The expression to recover the input voltage V_{in} is modified to:

$$
\begin{aligned}
V_{in} &= -\exp\left[\frac{V_{out} - b_{neg}}{M_{neg}}\right] && \text{if } V_{out} < 2.50 \\[2mm]
V_{in} &= \exp\left[\frac{V_{out} - b_{pos}}{M_{pos}}\right] && \text{if } V_{out} > 2.55
\end{aligned}
\tag{23}
$$

Table 6 Explosive Packages for the Lunar Seismic Profiling Experiment for Apollo 17. From Table 10-III in Kovach et al. (1973). See Haase et al. (2013) for estimates of the coordinates

Package No.	Explosive mass (kg)	Date	Time (UTC)
EP-6	0.454	Dec. 15, 1972	23:48:14.56
EP-7	0.227	Dec. 16, 1972	02:17:57.11
EP-4	0.057	Dec. 16, 1972	19:08:34.67
EP-1	2.722	Dec. 17, 1972	00:42:36.79
EP-8	0.113	Dec. 17, 1972	03:45:46.08
EP-5	1.361	Dec. 17, 1972	23:16:41.06
EP-2	0.113	Dec. 18, 1972	00:44:56.82
EP-3	0.057	Dec. 18, 1972	03:07:22.28

63 and 64 in digital units correspond to V_{in} of -0.00058 V and 0.00058 V respectively. Unfortunately, there is no point on the scale which corresponds to zero displacement. By looking at the traces, it is sometimes possible to infer where zero displacement occurs, and then artificially insert it. The following equation has zero displacement at 64 digital units:

$$V_{in} = -\exp\left[\frac{V_{out} - b_{neg}}{M_{neg}}\right] \qquad \text{if } V_{out} < 2.50$$
$$V_{in} = 0 \qquad \text{if } 2.50 < V_{out} < 2.55 \qquad (24)$$
$$V_{in} = \exp\left[\frac{V_{out} - b_{pos}}{M_{pos}}\right] \qquad \text{if } V_{out} > 2.55$$

We get better results using this modified equation, which adjusts the zero displacement on the seismometer to zero voltage. Calibration data are included in section S7 of the Electronic Supplement.

The Lunar Surface Profiling Experiment has the same transfer function as the active experiments (Eq. (19)), with different parameters (Table 7). As with the Active Seismic Experiment, we suspect that there was a pre-amplifier for the lower frequencies, but we have been unable to find the equation for it.

Table 7 also contains the parameters to recover the voltage input from the digital output (Eq. (21) and Eq. (24)), and the nominal sampling rate. Actual sampling rates obtained by Y. Nakamura during the period from 1976 to 1976 when the instrument was operating in listening mode ranged from 117.7773 Hz to 117.7803 Hz. Thus, the actual sampling rate was higher than the nominal rate shown in Table 7. A transfer function for one of the geophones is shown in Fig. 5.

2.4 Lunar Surface Gravimeter (LSG)

The Lunar Surface Gravimeter (LSG) was originally designed to detect gravitational waves on the Moon, as predicted from general relativity, and taking advantage of the very low noise conditions. The instrument was a high-sensitivity vertical accelerometer that sensed a local change in gravity. Unfortunately, the engineers miscalculated the compensating mass to deal with the reduced gravity on the Moon. Consequently, the instrument did not provide satisfactory data for its primary objectives. However, in addition to the primary objective, the LSG also functioned as a seismometer to detect ground motion. Recently, Kawamura et al. (2015) verified that the data quality were sufficient for seismic analysis. Kawamura

Table 7 Apollo 17 Lunar Seismic Profiling Experiment (LSPE) Sensor Parameters. The amplifier gain was estimated by Yamada (2012) using the system sensitivity at 10 Hz indicated in Kovach et al. (1973). The resonant frequencies and generator constants are from Table 10-I in Kovach et al. (1973). We obtained the conversion coefficient K_g, the conversion constant D and the logarithmic compression parameter values M_{neg}, M_{pos}, b_{neg}, b_{pos} and M_1 using calibration data originally provided by R. Kovach (via Y. Nakamura). We estimated the nominal values of the cutoff to the low-pass anti-aliasing filter fl and the damping constants, since these were not available in the original documentation. The sampling rate is from Table A1 in MSC (1971)

Parameter	Geophone No.			
	1	2	3	4
Resonant frequency (f_0 Hz)	7.38	7.31	7.40	7.35
Generator constant (G V/(m/s))	235.6	239.2	237.1	235.3
Damping constant (h)	0.7	0.7	0.7	0.7
Amplifier gain (A) at 10 Hz	495.2	467.2	477.9	482.3
Cutoff (f_l Hz)	30			
Conversion coefficient (K_g DU/V)	25.2609 ± 0.0235			
Conversion constant (D DU)	0.2876 ± 0.0672			
M_{neg}	$-0.2715 \pm 8.187 \times 10^{-6}$			
M_{pos}	$0.2681 \pm 7.086 \times 10^{-6}$			
b_{neg}	$0.4698 \pm 3.272 \times 10^{-5}$			
b_{pos}	$4.5260 \pm 3.068 \times 10^{-4}$			
Nominal sampling rate (Hz)	117.7667			

et al. (2015) used the additional data from the LSG to relocate the known deep moonquake source regions and also some previously unlocated farside deep moonquakes.

The Lunar Surface Gravimeter (LSG) used a Lacoste-Romberg type of spring-mass suspension to measure the vertical changes in local gravity and vertical ground motion. The sensor consisted of two fixed capacitor plates and a movable beam with another capacitor plate attached. The movable beam was attached to a zero-length spring, and thus small changes in the gravity field or ground motion changed the position of the beam. The position of the sensor beam could be adjusted to the proper equilibrium position using a ground command from Earth, and using an additional force applied by the caging mechanism. The movement of the sensor beam was recorded as a change in voltage which was then passed through an amplifier and a high-gain filter. The LSG had options for closed or open loop operation (Giganti et al. 1977). The closed loop contained a feedback mechanism, which was bypassed in open-loop mode. The instrument also had a free and seismic mode operation. Both modes could operate in either closed or open loop. The modes covered different frequency bands. The frequency band of the seismic mode overlaps with those of Apollo seismometers and can be directly compared with their data. We include a block diagram for the instrument in the Electronic Supplement.

Due to the malfunction, the LSG went through a series of operations to recover the functionality (see Giganti et al. (1977) and Kawamura et al. (2015) for more details). Initially, the sensor beam could not be centered to the equilibrium position. Additional force was applied to center the beam. This enabled the sensor beam to oscillate and the LSG was able to function as a seismometer. However, this also changed the sensitivity of the gravimeter from

its original design. The gravimeter was originally designed to have a flat response between 0.1 and 16 Hz in seismic mode. Instead, the gravimeter had a peaked response at around 1.9 Hz, and sensitivity at low frequencies was degraded significantly after the recovery operation. The data were sampled at the same sampling rate as the short-period seismometers ($\sim .02$ s).

The Lunar Surface Gravimeter (LSG) was changed to open loop mode with maximum seismic output on December 7, 1973 (Giganti et al. 1977). Consequently, all of the available data were recorded in this mode. The transfer function for open seismic mode is as follows:

$$A_{LSG}(\omega) = S(\omega) G_{dc} K_s G_a G_s F_l(\omega) F_h(\omega) \quad \frac{V}{(m/s^2)} \tag{25}$$

where $S(\omega)$ is a transfer function of the seismometer for acceleration (Eq. (7)). We defined the transfer function using the block diagram in Fig. 2 of Weber and Larson (n.d.) The diagram is reproduced in the electronic supplement. G_{dc} is a DC coupled gain, which is missing from the block diagram but described in p2, Weber and Larson (n.d.). K_s is the sensitivity of the displacement transducer, G_a is the adjustable gain which varied from 1 to 86.4 in 16 discrete steps (Fig. 2, Weber and Larson n.d.). G_s is the seismic-mode amplifier gain. $F_l(\omega)$ is a low-pass filter, and $F_h(\omega)$ is a high-gain high-pass filter.

The experiment used an 8th-order low-pass Butterworth filter (described in Eq. (20)). It also used a high-gain 4th-order high-pass Butterworth filter as follows:

$$F_h(\omega) = \frac{G_1}{\sqrt{1 + \left(\frac{\omega_h}{\omega}\right)^{2m}}} \tag{26}$$

where G_1 is the gain, m is the order of the filter, and ω_h is the cutoff angular frequency.

After the corrections were made, the quality factor was estimated to be about 25, instead of being critically damped (p1, Weber and Larson n.d.). Using $1/(2Q)$, this gives a damping ratio h of 0.02. The natural angular frequency ω_0 was lowered to around 12 rad/s (p3, Weber and Larson n.d.). Using $\omega_0/(2*\pi)$, this gives an approximate value of 1.90986 Hz for the natural frequency f_0. The adjustable gain G_a was set to 64.0 from day 116 of the mission (p3, Weber and Larson n.d.). The scale bar in Fig. 5 of Weber and Larson (n.d.) shows that 1 digital unit was 20 mV. The reciprocal value gives 50 DU/V for K. The block diagram in Fig. 2 of Weber and Larson (n.d.) shows values for: the displacement transducer K_s (56.3 V/m); the cut-off for the low-pass filter f_l (16 Hz); the gain of the high-gain filter G_1 (1900); the seismic-mode gain G_s (1.5); the cut-off for the low-pass filter f_l (16 Hz).

We estimated the order for the high and low-pass filters, and the cutoff frequency for the high-pass filter using the transfer function produced by the original team (Fig. 5, Weber and Larson n.d.). Finally, the conversion K between volts and digital units (DU/V) is applied. Although we reproduce the peak at 1.9 Hz, we were unable to reproduce the sharp peak in the original. Since the instrument had to be adjusted after deployment, we stress that many of the parameters described here are only estimates.
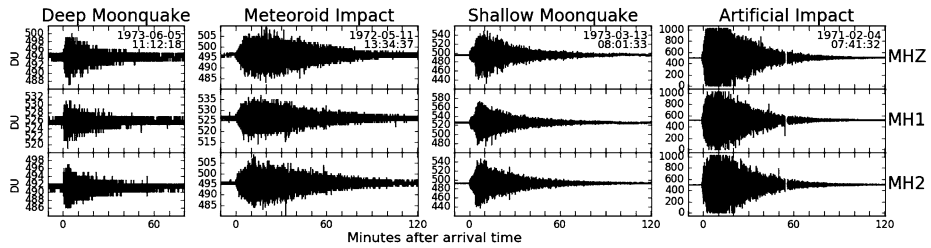
$$f_0 = 1.90986 \text{ Hz}$$

$$h = 0.02$$

$$G_{dc} = 21$$

$$K_s = 56.3 \text{ V/m}$$

$$G_a = 64.0$$

Fig. 7 Examples of a Deep Moonquake, a Meteoroid Impact, a Shallow Moonquake and an Artificial Impact Event. The events were recorded at seismic station S12 on 3 components (MHZ, MH1 and MH2). Timing is relative to the first arrival, which is indicated on each of the events. The y-axis scale is in digital units (DU), and the scale is different for each of the events. On the highest amplitude signal (the artificial impact) the signal was clipped

$$G_s = 1.5$$

$$K = 50 \text{ DU/V}$$

$$\text{Sampling Rate} = 53 \text{ Hz, nominal}$$

The filter parameters have the following values:

$$G_1 = 1900$$

$$f_h = 2 \text{ Hz}$$

$$\omega_h = 12.57 \text{ rad/s } (2\pi f_h)$$

$$f_l = 16 \text{ Hz}$$

$$\omega_l = 100.53 \text{ rad/s } (2\pi f_l)$$

$$n = 4 \text{ (4th order filter)}$$

$$m = 8 \text{ (8th order filter)}$$

The estimated transfer function for the Lunar Surface Gravimeter is shown in Fig. 3. After the malfunction and reconfiguration, the average noise level of the Lunar Surface Gravimeter (LSG) was higher than the other Apollo seismometers (Lauderdale and Eichelman 1974).

3 Seismic Sources

Seismologists have observed and categorized several types of moonquakes. These include deep moonquakes, meteoroid impacts, shallow moonquakes, thermal moonquakes and also artificial impacts (Fig. 7; Table 8; Schematic in Fig. 5 of (Garcia et al. 2019)). Many of these quakes are observed on both the mid-period instruments and the short-period instruments. Most thermal moonquakes can only be seen on the short-period instruments. Figure 6 in our companion paper (Garcia et al. 2019) shows maps of estimated locations.

Lunar events typically have a very long duration, and indirect scattered energy can arrive tens of minutes after the direct waves (e.g. Fig. 7). The scattered energy is known as the seismic coda. These long, reverberating trains of seismic waves were interpreted as scattering in

Table 8 Number of moonquakes of each different type detected and cataloged by Nakamura et al. ([1981](#)) and updated in 2008 with minor corrections in 2018. These events were detected on the mid-period instruments

Type of moonquake	No.
Artificial impacts	9
Meteoroid impacts	1743
Shallow moonquakes	28
Deep moonquakes (assigned to nests)	7083
Deep moonquakes (not assigned to nests)	317
Other types (including thermal quakes)	555
Unclassified	3323
Total	**13058**

a surface layer overlying a non-scattering elastic medium (e.g. Dainty et al. [1974](#)). Diffusion scattering is important when the mean free path (the average distance seismic energy travels before it is scattered) is short compared to the seismic wavelength. In comparison with terrestrial environments, Dainty and Toksöz ([1981](#)) showed very short mean free paths for the Moon. Dainty et al. ([1974](#)) and Aki and Chouet ([1975](#)) distinguished the diffusion model of seismic wave propagation (which applies to a strongly scattering medium) from a single scattering model (which applies to a weakly scattering medium). The much larger amplitude (relative to direct phases) and much greater duration of lunar seismograms compared to terrestrial seismograms suggests both more intense scattering and much lower attenuation on the Moon than on the Earth (Dainty and Toksöz [1981](#)). Sato et al. ([2012](#)) provide an extensive review of the theoretical developments in the field of scattering and attenuation of high-frequency seismic waves (particularly when applied to the Earth).

3.1 Artificial Impacts

Nine impacts occurred when the Saturn third stage boosters or the ascent stages of the lunar module were deliberately crashed into the Moon. These observations are particularly valuable, since the timing of the impact, the location, and the impact energy are known (see Section S9 in the electronic supplement). Unfortunately, the tracking was prematurely lost for Apollo 16's Saturn booster, meaning that both the location and timing were poorly known for this impact. Plescia et al. ([2016](#)), Wagner et al. ([2017](#)) and Stooke ([2017](#)) estimated the location of many impacts using remarkable images from the camera on Lunar Reconnaissance Orbiter. Photographs of the impact craters can be viewed online (LROC [2017](#)).

3.2 Meteoroid Impacts

More than 1700 events recorded during the operation of the Apollo stations were attributed to meteoroid impacts (e.g. the Nakamura et al. ([1981](#)) catalog, provided within the electronic supplement). Oberst and Nakamura ([1991](#)) found two distinct classes of meteoroids impacting the Moon, originating from either comets or asteroids, and estimated the mass for the meteoroids to range from 100 g to 100 kg.

The waveforms of meteoroid and artificial impacts differ significantly from fault-generated quakes. They do not have a double-couple source. Since the Moon has no significant atmosphere, impacts have high velocities, and the impactor tends to fragment and vaporize. Teanby and Wookey ([2011](#)) noted that this leads to the creation of radially symmetric craters, except for very low-angle impacts (with respect to the horizontal). Therefore,

the most appropriate seismic source is purely isotropic (explosive) (Stein and Wysession 2003; Teanby and Wookey 2011; Lognonné and Kawamura 2015). Gudkova et al. (2011) modeled the impacts using the seismic impulse. They estimated the masses of the impacting meteoroids by calibrating the model with the known masses of the artificial impacts.

Meteoroid impacts are clearly of exogenic origin. Since the impacts are surface events, seismic waves propagate through the regolith and megaregolith layer twice, once at the source and another below the seismic station. This results in different scattering features and generates more gradual signal onset and longer coda compared with shallow and deep moonquakes. While some experiments have studied the seismic features of impacts (e.g. McGarr et al. (1969) and Yasui et al. (2015)), observations from Apollo are still the only example of impacts on a body without an atmosphere and provide a unique opportunity to investigate the source mechanism. Daubar et al. (2018) includes a review of lunar impacts.

3.3 Shallow Moonquakes

Shallow moonquakes are rare events (with only 28 events in the catalog of Nakamura et al. (1981)), which have larger magnitudes than the other naturally occurring events. There is some variation in the estimated depth ranges for these events. In the VPREMOON model of Garcia et al. (2011), they occur at depths from 0 to 168 km. In contrast, Khan et al. (2000) preferred a depth range of 50 to 220 km, and suggested that they occur in the upper mantle. Similarly, Nakamura et al. (1979) suggested that the amplitude decay function of shallow moonquakes implies that they are likely to be located shallower than 200 km depth but deeper than the crust-mantle boundary. Oberst (1987) estimated the equivalent body-wave magnitudes to be between 3.6 and 5.8. He also estimated unusually high stress drops. Shallow moonquake spectra include high frequencies, which are clearly visible on the short-period seismographs. While the deep moonquakes have little seismic energy above 1 Hz, energy for the shallow moonquakes continues up to about 8 Hz and then rolls off. This is the reason that shallow moonquakes were initially called high-frequency teleseismic events. No correlation between shallow moonquakes and the tides has been observed (e.g. Nakamura (1977)). Nakamura (1980) showed a strong similarity between these quakes and intraplate earthquakes on Earth, particularly considering the relative abundance of large and small quakes.

3.4 Deep Moonquakes

Deep Moonquakes are the most numerous events, and are found at depths from 700 to 1200 km (Nakamura et al. 1982; Nakamura 2005). They have highly repeatable waveforms, suggesting that they originate from source regions (or 'nests') which are tightly clustered. The quakes have been classified into numbered groups or clusters (e.g. Nakamura 1978; Bulow et al. 2007; Lognonné et al. 2003). The exact number of nests varies between studies, but Nakamura (2005) identifies at least 165 different source regions, mainly on the nearside of the Moon. The largest group, A1, contains over 400 quakes. Gagnepain-Beyneix et al. (2006) found that the A1 group was large enough to distinguish subgroups of events with slightly different waveforms. When they processed the stacks separately, the final waveform stacks of these subgroups were somewhat different, but the delays between P and S arrival times obtained by correlation implied that the distance between sources was at most one kilometer. Nakamura (2003) correlated every pair of events using a single-link cluster analysis. Events belonging to one source region correlated to a high degree, while those belong to separate source regions correlated to a lesser degree. A surprising finding was that some

events that were originally thought to be belonging to two separate source regions were found to be highly correlated.

Many studies, including Lammlein et al. (1974), Lammlein (1977) and Nakamura (2005), have noted an association between the occurrence times of deep moonquakes and the tidal phases of the Moon. Analysis of the periodicity of deep moonquake occurrence shows the strongest peak at 13.6 days, followed by a peak around 27 days (e.g. Lammlein 1977). Additional 206-day variation and 6-year variation, due to tidal effects from the Sun, are also observed (Lammlein et al. 1974; Lammlein 1977). However, analysis of individual clusters by Frohlich and Nakamura (2009) shows tidal periodicity for each cluster, but not necessarily the same dependence on the tidal cycle for all clusters.

Although the deep moonquakes appear to be tidally triggered, the exact cause remains unclear. Saal et al. (2008) argued that the presence of fluids (especially water) explained the mechanism. Instead, Frohlich and Nakamura (2009) favored partial melts. Kawamura et al. (2017) calculated stress drops from deep moonquakes of 0.05 MPa, which is similar to shear tidal stresses acting on deep moonquake faults. They argued that the tidal stress not only triggers the deep moonquake activity but also acts as a dominant source of the excitation. As shown in Fig. 5 of our companion paper (Garcia et al. 2019), deep moonquakes occur approximately half way to the center of the Moon. Calculated tidal stresses are strongest from 600–1200 km, which covers the range of estimated deep moonquake depths (e.g. Cheng and Toksöz 1978).

The majority of the deep moonquakes have been located to the nearside of the Moon, with around 30 nests attributed to the farside (Nakamura 2005)). Since none of the events have been located to within about 40 degrees from the antipode of the Moon, Nakamura (2005) suggested that this region of the farside is aseismic, or alternatively that the very deep interior of the Moon severely attenuates or deflects seismic waves.

3.5 Thermal Moonquakes

Duennebier and Sutton (1974) showed that the majority of the many thousands of seismic events recorded on the short-period seismometers were small local moonquakes triggered by diurnal temperature changes. More recently, Dimech et al. (2017) found and categorized 50,000 events recorded by the Lunar Seismic Profiling Experiment at Apollo 17. The events occurred periodically, with a sharp double peak at sunrise and a broad single peak at sunset.

4 Compilation of Reference Data

We have compiled reference data from various sources, and provide these data sets within the Electronic Supplement. This section describes these data sets.

4.1 Deep Moonquake Stacks

As described above, waveforms from each deep moonquake source region are highly repeatable. Researchers have used the repeatability of the waveforms to use stacking and cross-correlation methods to enhance the signal-to-noise ratio. It is easier to pick the arrival times on the stacked waveforms, which are considerably clearer. The quality of the stack will depend on a number of factors including the number of stacked events, the signal-to-noise ratio of the individual events and the filtering applied. Nakamura (1978) showed that source

regions also produce events with similar waveforms but with flipped polarity. He suggested that this was caused by similar events being triggered by different parts of the tidal cycle.

In section S2 of the Electronic Supplement, we provide deep moonquake stacks from three independent sources in miniSEED format (Nakamura 2005; Lognonné et al. 2003; Bulow et al. 2007).

Nakamura (2005) correlated deep moonquakes to determine clusters, and stacked the seismograms when he detected 10 or more events within a cluster. The individual traces were weighted to maximize the final signal-to-noise ratio. The stacks were made from cross-correlations between events using single-link cluster analysis. He made P and S arrival time picks and estimated hypocenters for many of the stacks. Using a slightly different process, Lognonné et al. (2003) stacked seismograms after time alignment relative to a reference event. Bulow et al. (2007) also stacked these data, which were originally included in Bulow et al. (2005). They used a median-despiking algorithm to produce improved differential times and amplitudes, which enabled them to produce cleaner stacks.

Lognonné et al. (2003) recorded which event was the reference in the header to the file. However, Nakamura (2005) did not use reference times in his process, and we do not have reference times from Bulow et al. (2005). This unfortunately makes it more difficult to compare stacks or calculate arrival times. For the stacks provided in the Electronic Supplement, we are unable to confirm exactly which individual events were used in each stack, which traces of which individual events were flipped relative to the reference event, and the filtering or pre-processing carried out by the researchers. We expect that slightly different criteria were used by different researchers to accept or reject each trace. The stacks of Nakamura (2005), Bulow et al. (2007), and Lognonné et al. (2003) are 500 s, 4200 s and 1600–3500 s long, respectively.

Figure 8 shows three examples of stacked deep moonquake clusters, from A1, A40 and A97, from three independent sources. These clusters were selected to show both good and bad examples. Both the A1 and A40 stacks show good coherence between the stacks, with correlation coefficients between 0.81 and 0.96. The correlation windows are 300 s and begin at the P-arrival pick for A01 and 50 s before the S-pick for A40 and A97. Only the vertical component (Z) is available for the A97 stack. For A97, the Bulow et al. (2007) and Nakamura (2005) stacks align with a correlation coefficient of only 0.59, and the Lognonné et al. (2003) stack does not align with the other stacks without post-filtering. The catalog includes 442, 65 and 62 events for the A1, A40, and A97 clusters, respectively. A1 contains the largest number of events with good signal-to-noise ratio, followed by A40. Since the different studies used different reference traces, several of the stacked traces were of reverse polarity. For example, for the A1 cluster MH1 and MH2 from Bulow et al. (2007) and all three traces from Nakamura (2005) were of reverse polarity to those from Lognonné et al. (2003). The reverse traces were flipped before calculating the correlation coefficients or plotting.

Figure 9 shows the correlation coefficients between pairs of studies, for each available named cluster. Many pairs of stacks have correlation coefficients greater than 0.85. However, there are also many pairs which do not correlate. The correlations are affected by the number of events in the stack, the length of the stacking window, as well as the filtering applied. In addition, different events may be chosen (or excluded) by different studies.

## 4.2 Lunar Catalog of Arrival-Time Picks

We compiled arrival times from Goins (1978), Horvath (1979), Nakamura (1983), Lognonné et al. (2003), Bulow et al. (2007) and Zhao et al. (2015)). We provide the arrival times within
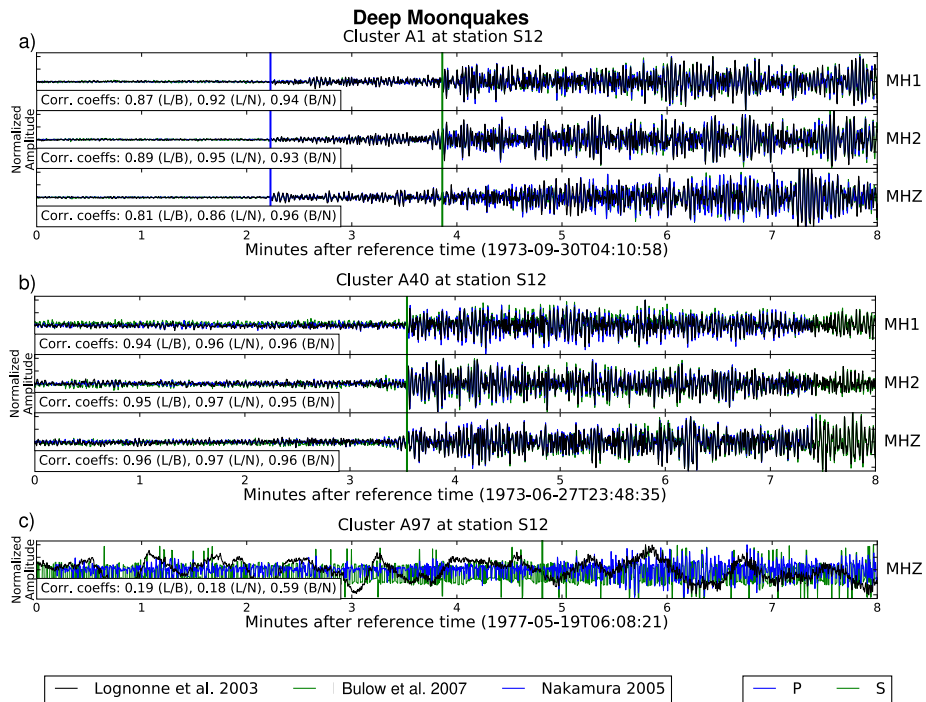
Fig. 8 Examples of deep moonquake stacks from **a**) A1, **b**) A40 and **c**) A97, and from three independent sources (Lognonné et al. 2003; Bulow et al. 2007; Nakamura 2005). We aligned the independent stacks using cross-correlation. The correlation coefficients for each pair are shown in the boxes. The reference times are from Lognonné et al. (2003), and are shown beneath each stack. The plot shows S wave arrivals (green lines), and P wave arrivals (blue line; only available for the A1 cluster) from Lognonné et al. (2003). For A97, the Bulow et al. (2007) and Nakamura (2005) stacks align with a correlation coefficient of only 0.59. The Lognonné et al. (2003) A97 stack does not align with the other stacks without post-filtering the stack. The correlation windows are 300 s and begin at the P-arrival pick for A01 and 50 s before the S-pick for A40 and A97

section S3 of the Electronic Supplement. The P and/or S arrivals were picked for artificial impacts, meteoroid impacts, shallow moonquakes, and deep moonquake stacks. Nakamura (1983) summarized the published results of Horvath (1979) and Goins (1978) along with previously unpublished results from J. Koyama resulting in arrival times from 8 artificial impacts, 18 meteoroid impacts, 14 shallow moonquake events, and 41 deep moonquake stacks. Lognonné et al. (2003) picked arrivals for 27 impacts (8 artificial), 8 shallow moon-quake events, and 24 deep moonquake stacks. Bulow et al. (2007) picked arrivals from 9 deep moonquake stacks.

The location of each event was determined using the arrival times of the S and P waves coupled with velocity models of the Moon's interior. The locations of the artificial impacts are known and provided constraints for the inversion of the velocity structure of the crust and upper mantle (Nakamura 1983). In contrast, the source locations for the other quakes rely on previously determined models. Garcia et al. (2019), also written by our group, provides a discussion of the determination of the source locations. We provide two possible origin locations. One set of locations come from Lognonné et al. (2003). The second set comes
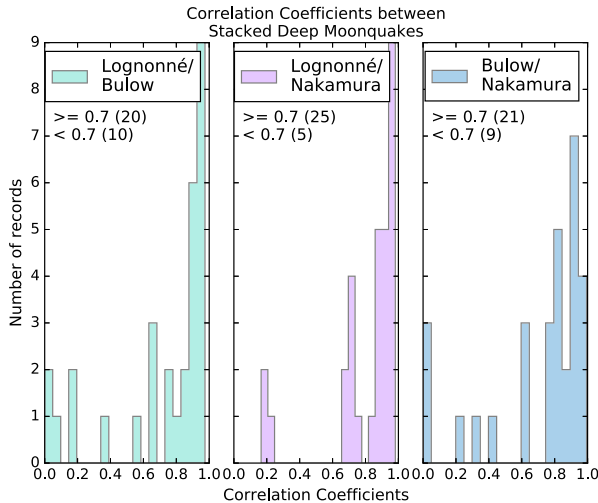
Fig. 9 Histogram of the correlation coefficients between the vertical component of the stacked deep moonquake traces for each named cluster compiled by different authors. Turquoise lines compare Lognonné et al. (2003) and Bulow et al. (2007); purple lines compare Lognonné et al. (2003) and Nakamura (2005); blue lines compare Bulow et al. (2007) and Nakamura (2005). The number of clusters with correlation coefficients greater than 0.7 or below 0.7 is shown. Correlation window length is 300 s, and begin 50 s before the S-arrival time pick, when it is available. When the S-arrival has not been picked, the window length is the full length of the shortest trace

from Garcia et al. (2011), and were calculated using the velocity model Very Preliminary Reference Moon (VPREMOON).

For individual events, such as shallow moonquakes or impacts, a reference timestamp is provided. However, the P and S arrival times of the deep moonquakes are picked on stacked waveforms for which a single reference time is not always available. Unfortunately, different studies used different reference events to align their stacks. We decided to present here only arrival times of deep moonquake events for which a quake location is available. When the deep moonquake stacks used the same reference time as Lognonné et al. (2003), the P and S arrival times are provided. When the deep moonquake cluster is not clearly identified as the one used in Lognonné et al. (2003), the P and S arrival times are provided with their own reference time. When the arrival time does not have a clear reference date and time, or a different one from Lognonné et al. (2003) for the same deep moonquake cluster, only S-P differential travel times are provided.

Later studies of deep moonquakes, such as Bulow et al. (2007), were able to include 503 more individual events than Nakamura et al. (1981). By using cross-correlation to identify new events, some moonquake stacks had up to 53% more events than Nakamura et al. (1981). The compiled arrival times relative to the reference time, and the S-P times when a reference time is not available, are provided in Section S3 of the electronic supplement. For some events, there were arrival times from multiple stations and from multiple studies. In the instances where more than two studies cite P, S, and/or (S-P) values for an event, we computed the mean and standard deviations.

Figure 10 shows P and S arrival times from Lognonné et al. (2003), plotted by epicentral distance. The plot shows some scatter for both P and S arrival times. We expect some scatter in this plot, since the events are estimated to originate from different depths. In addition,
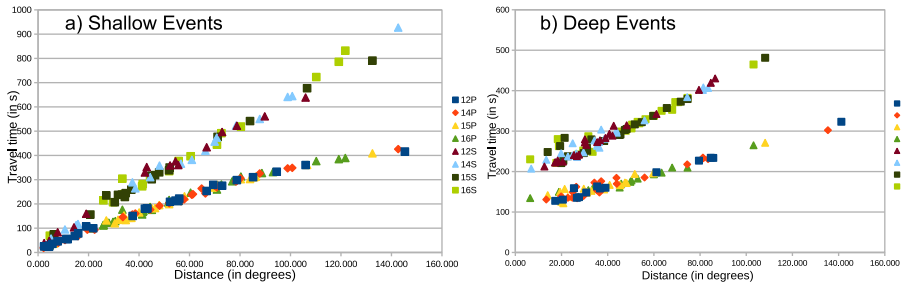
Fig. 10 Travel times of events as a function of epicentral distance (in degrees). The left panel shows shallow events (natural impacts, artificial impacts and shallow moonquakes) and the right panel shows deep events. The times are the median values extracted from the whole travel-time database (included in the electronic supplement). They were used as input data for the inversion tests presented into our companion paper (Garcia et al. 2019). Error bars are available but not presented for clarity

it may be difficult to estimate epicentral distance. Some variation is also expected from differences in crustal thickness or seismic velocities between different regions of the Moon.

4.2.1 Statistical Analysis

The accuracy of measuring the arrival times of both the P-wave and S-wave for different events strongly affects the travel-time measurement, which is the key parameter for further inversions on both source location and velocity structure. However, due to the signal characteristics of the lunar seismic records, accurate and reliable arrival-time measurements are challenging. The arrival times of artificial impacts and deep moonquakes can have large differences between different studies. For example, for the impact of Apollo 15's Lunar Module (15LM), the P-wave arrival time from Nakamura (1983) is 5.5 s earlier than that of Lognonné et al. (2003).

We calculated the variation of arrival-time picks (Fig. 11). Since we calculate a mean for each event, we require at least two independent observations. Where available, we show P arrivals, S arrivals, and the difference between the S and P arrival times (S-P time). For the P arrivals, the small number of artificial impacts show high consistency (the standard deviation is 1.3 s). The second lowest standard deviations are for the shallow moonquakes (3.0 s), followed by the meteoroid strikes (4.0 s) and a small number of deep moonquake observations (10.1 s). In general, the S arrivals have lower consistency than the P arrivals. There are too few observations for meaningful statistics for the artificial impacts for S and also S-P. The standard deviations are lowest for the stacked deep moonquake events (3.7 s), followed by the shallow moonquakes (13.2 s) and then the meteoroid strikes (18.2 s). Large outliers over 40 s are common for both the shallow moonquakes and the meteoroid strikes. Naturally, the S-P times reflect the uncertainties in both measurements, and the meteoroid, shallow and deep events all have standard deviations greater than 11 s. Lognonné et al. (2003) estimated errors for the picked arrivals for some of their events of 1 s, 3 s and 10 s, for high, intermediate and low quality events. The spread between independent observations suggests that the original error estimates may be too small.

4.3 Arrival Time of the Maximum Energy and the Coda Decay Time

Lunar seismograms are characterized by strongly scattered waves with a long duration, when compared with their terrestrial counterparts. The coda, which can be thought of as the tail

Fig. 11 Histograms of the differences between arrival time picks from different catalogs, plotted relative to the mean of all picks for the event


Arrival Time Residuals (relative to mean)
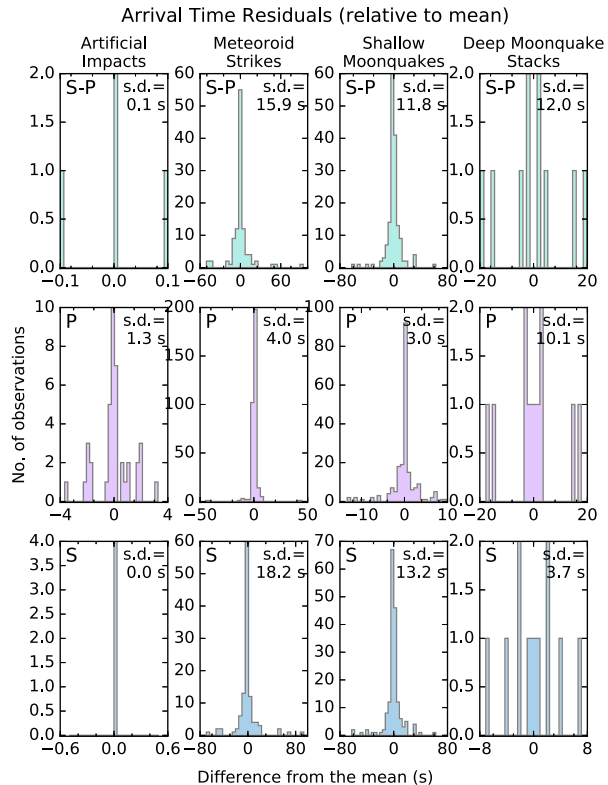
of the seismogram, is formed from the scattered waves which arrive after the direct waves. There is a long delay time between the onset of the signal and the arrival of the maximum energy, also known as the rise time (Latham et al. 1971; Blanchette-Guertin et al. 2012). A long rise time indicates multiple scattering in a strongly heterogeneous medium, and that the waves are strongly dispersed. The rise is followed by an even longer decay time, where energy from the scattered waves continues to arrive at the seismic station. An accurate measurement of the rise time requires an accurate pick of the S-wave arrival, which is not always possible. Instead, Gillet et al. (2017) used t_{max}, which is the time elapsed from the energy release at the source (at time t_0) to the arrival of the maximum of the energy (Fig. 12). Although measurement of t_{max} does not require a pick of the S-wave arrival, it is affected by any error in the estimation of the origin time t_0.

The long duration of the coda on the Moon is the result of a very low noise level and significantly lower anelasticity than Earth. Using the diffusion model of scattering of Dainty et al. (1974) and Aki and Chouet (1975), we can quantify the decay of a seismogram after the arrival of the maximum energy. Aki and Chouet (1975) introduced a quality factor Q_c, such that the energy varies in the coda as

$$t^{-\alpha} \exp(-\omega t / Q_c) \tag{27}$$

where ω is the central frequency of the signal, t is the time elapsed since the energy release at the source and α is an exponent which depends on the geometry of the scattering medium. Alternatively, Blanchette-Guertin et al. (2012) introduced a characteristic decay time of the
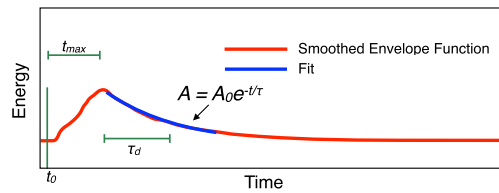
Fig. 12 Schematic diagram showing the smoothed envelope function for an example event, and the fit to the coda decay. t_{max} is the lapse time between the origin time of the event (t_0) and the maximum of the energy at a given seismic station. τ_d is the characteristic decay time (the time taken for the smoothed envelope to decay to $1/e$ of its original value). It is determined with a linear regression of the logarithm of the energy as a function of the lapse-time t. A_0 is a constant (although we do not determine its value)

coda as

$$\tau_d = Q_c/\omega \tag{28}$$

On Earth, the exponent is usually chosen between 1 and 2 depending on the geological context and the wavefield content. In the case of the Moon, the dissipation is so weak and the propagation time is so long that waves have the time to explore the entire volume of the planet. In such a scenario, one expects the signal to simply decay exponentially at long lapse time, thereby suggesting $\alpha = 0$ (Blanchette-Guertin et al. 2012; Gillet et al. 2017). We also adopt this value. τ_d is the time taken for the (smoothed) coda to be reduced to $1/e$ times its initial value.

Observations by Latham et al. (1971), Dainty et al. (1974) and others show that the shape of the envelope on the seismogram depends strongly on the filtering applied to the signal. This implies that both t_{max} and τ_d vary as a function of frequency. Furthermore, multiply-scattered wavefields typically show large fluctuations. The interference of a large number of scattered waves following different complicated paths results in Gaussian fields. This property may be understood as a consequence of adding a large number of random phasors in the framework of the Central Limit Theorem, where each phasor conveys the amplitude and phase of a given scattering path (see Goodman (2015) for further details). Gaussianity implies that if one observes the coda in a time window which is large compared to the central period of the signal, yet small compared to the coda decay time, the displacement field obeys a Gaussian distribution with zero mean and a variance equal to the mean intensity of the signal in the selected time window. This property is readily verified on real data (e.g. Anache-Ménier et al. 2009). The intensity (the squared field) follows an exponential distribution, provided that it is considered within a time window long enough to include many signal cycles, but short compared to the decay time. Consequently, although the original field appears 'noisy', it can be smoothed to give the coda envelope. These two remarks indicate that both filtering and smoothing are key steps in the analysis of seismogram envelopes.

A typical choice of filter is the 4-pole Butterworth with a bandwidth equal to 2/3 of the central frequency (Aki and Chouet 1975). The next step is to convert amplitude to energy. The simplest procedure is to square the filtered traces which directly yields a quantity proportional to the kinetic energy of wave motion. Finally, the squared trace is smoothed to reduce the fluctuations. A customary choice is to apply a moving-average filter with a typical duration of 8 to 16 periods. Longer windows provide smoother envelopes at the expense of reducing the signal dynamics.
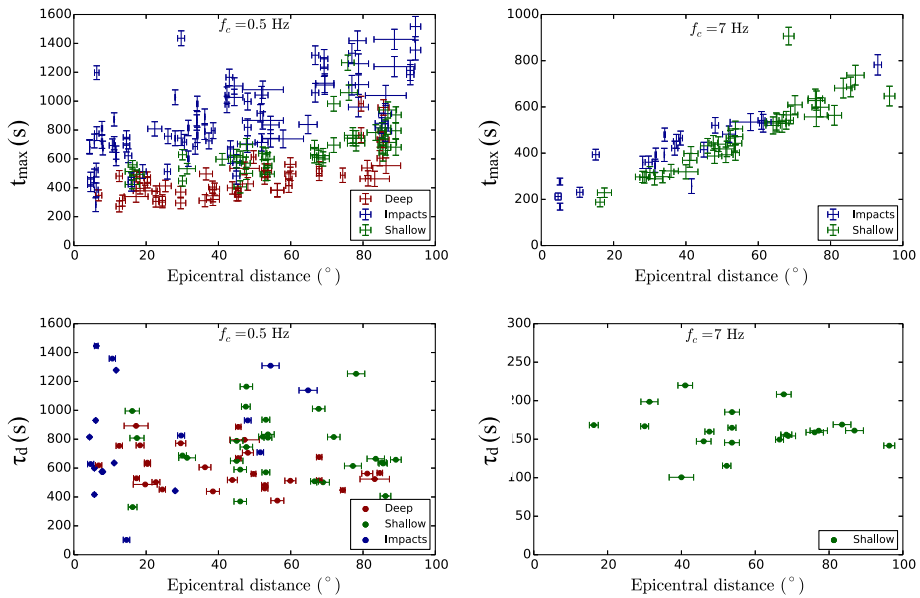
Fig. 13 Measurements of the arrival time of the maximum t_{max} (top) and the characteristic coda decay time τ_d (bottom) at low frequency (0.5 Hz, left) and high frequency (7 Hz, right). Error bars show the uncertainty of the measurements. Colors refer to the type of events (see inset). Compiled using data from Gillet et al. (2017)

Once smooth energy envelopes have been obtained, it is straightforward to find the maximum of the energy and its associated time of arrival. Estimating the uncertainty is difficult due to residual random fluctuations of the envelope. Gillet et al. (2017) describe a suitable procedure based on the statistics of Gaussian random fields. An estimate of τ_d may be obtained straightforwardly by performing a linear regression to the logarithm of the energy as a function of the lapse-time. The choice of the time window on which this operation is performed is critical. Different windows generally yield different estimates. For this reason, it is important to specify the coda time window and to calculate a goodness of fit parameter for the linear regression such as the correlation coefficient. In this work, the length of the coda window is 500 s and τ_d measurements with a correlation coefficient lower than 0.95 are not shown. The starting time of the coda window is provided for each trace in the electronic supplement.

Figure 13 shows measurements of t_{max} and τ_d performed in two frequency bands centered around 0.5 Hz and 7 Hz. t_{max} generally increases with epicentral distance for both low and high frequencies. Deep moonquakes have the lowest t_{max} for a given epicentral distance, followed by shallow moonquakes and then impacts. t_{max} could not be measured for the deep moonquakes at high frequencies. Modeling (at 0.5 Hz) predicts a dependence of t_{max} on epicentral distance, as well as a sharp increase in t_{max} around 10° epicentral distance for the impacts (Fig. 7, Gillet et al. (2017)). Note that t_{max} combines the travel time for the initial energy, as well as the rise time from initial energy to maximum, and that both quantities depend on epicentral distance.

Figure 13 does not show a clear dependence of the characteristic decay time τ_d on epicentral distance for either high or low frequencies, and measurements could not be made at high frequencies for either the deep moonquakes or the impacts.

🖄 Springer

5 Final Remarks

5.1 Locating Lunar Events and Internal Structural Models of the Moon

In a companion paper, (Garcia et al. 2019), our group has analyzed event locations, input geophysical data, prior information and previously published internal structural models of the Moon. The seismic velocity models reviewed do not reach a consensus on the crustal thickness or the lunar structure below 1200 km depth. The remaining features are consistent among various publications. A detailed review of studies inferring attenuation and scattering properties inside the Moon is also presented. It demonstrates that the various authors agree on a very low intrinsic attenuation inside the Moon and strong scattering of seismic energy within the lunar crust and upper mantle. A review of the seismic source locations is also presented. Locations vary significantly among studies, particularly for the depth of deep moonquakes. Finally, the P and S arrival times collected through this study have been inverted with three different model parameterizations to infer the effect of model parameterization on the seismic velocity model obtained. Although there are some differences between the three models, they all present a low velocity region in the 100–250 km depth range. Our group ascribe this feature to a temperature gradient around 1.7 °C/km. This may be driven by the close proximity to the Procellarum KREEP Terrane, a geological region which dominates the lunar nearside, and which contains high abundances of heat-producing elements.

5.2 Low Level Requirements for an International Lunar Network of Geophysical Sensors

As described above, various initiatives around the world are targeting new geophysical deployments on the lunar surface. These projects are renewing the old idea of having an International Lunar Network (ILN) of geophysical instruments operating simultaneously on the Moon. However, in order to be able to analyze the data of these simultaneously operating instruments as a network, the missions/instruments/sensors need to fulfill a minimum set of requirements. Our team sets out these minimum requirements in Fig. 14. The requirements are built upon a single objective: to ensure the capability of researchers to analyze data simultaneously acquired by similar geophysical sensors on the Moon. These requirements do not only apply to seismic sensors but to any geophysical sensors deployed on the Moon. For each requirement, we justify the flow-down from science objectives to station/mission and instrument/sensor requirements. However, performance requirements are not specified in order to allow low performance sensors to still fulfill these requirements. Therefore, decisions on performance considerations can be decided by the organization funding the instrument or the mission. The science return as a function of instrument performance is not considered in these requirements because it often depends not only on sensor self noise, but also on mission design, deployment capabilities, and many other factors.

5.3 Resources within the Electronic Supplement

Section S1 contains parameters describing the location of the Apollo passive seismometers, including longitude, latitude, elevation, azimuth of the horizontal seismometer components and distance between stations. Section S2 contains stacked traces from deep moonquake clusters from three independent studies, in miniSEED format. Section S3 contains arrival-time catalogs from six independent sources, as well as estimates of event time and location where available. Section S4 contains the full lunar catalog which contains over 13,000

Low Level Requirements for an International Lunar Network
Specified by:
ISSI Team: An International Reference for Seismological Data Sets and
Internal Structural Models of the Moon

Major Requirement #	Requirement #	Topic	Requirement	Comments
			WARNING: These requirements must be applicable to any instrument type (geophone, seismometer, VBB seismometer etc) and any mission type (hard or soft lander) from any agency (NASA, CNSA etc).	
OBJECTIVE				
	ILN-REQ-0	Interoperability of Stations for Network Analysis	Data from geophysical stations deployed on the Moon must allow an international community of researchers to locate events, perform waveform analysis and develop structural models.	These requirements cover seismic mic data. Additional requirements should be stated for sensors sensing ground temperature, gravity field, magnetic field, ground rotations, low frequency planetary scale rotations and deformations, and lunar laser ranging.
SCIENTIFIC AIMS				This section outlines the reasons for the requirements in the following sections. In defining the requirements, we make the assumption that the internal structure is perfectly known.
ILN-REQ-0	ILN-REQ-0.1	Source Timing	The origin time of geophysical events detected by the seismic network must be recovered with an accuracy better than the sampling rate of the recording stations.	
ILN-REQ-0	ILN-REQ-0.2	Source Location	The source location of geophysical events detected by the network must be recovered with an accuracy better than a quarter of the wavelength of the signals used to locate the source.	
ILN-REQ-0	ILN-REQ-0.3	Source Energy	The energy of the source of geophysical events detected by the network must be recovered with an accuracy better than 20%.	
ILN-REQ-0	ILN-REQ-0.4	Source Radiation	The radiation pattern of the geophysical sources detected by the network must be recovered with an accuracy better than 10°.	
ILN-REQ-0	ILN-REQ-0.5	Data Access	Proper recording and archiving of all data and metadata is necessary to allow scientific analysis by an international community of researchers.	

Fig. 14 Minimum requirements for an international lunar network—version 1-0

		STATION REQUIREMENTS		We place the following limits on the back propagation of errors into new models of the Moon, which could arise from poor time synchronization or lack of station information etc.
ILN-REQ-0.1	ILN-REQ-1.1	Source timing: back propagated error level = X*dt	Time synchronization between stations must be provided with an accuracy that ensures that timing errors for the geophysical signals are smaller than the sampling rate of the sensor.	
ILN-REQ-0.2	ILN-REQ-1.2	Source location: back propagated error level = X * max wavelength	Station information must be provided with an accuracy that ensures that the errors on the location of the source of geophysical signals are smaller than a quarter of a wavelength of the signal used for finding the location.	
ILN-REQ-0.3	ILN-REQ-1.3	Source energy = X%	Characteristics of instruments deployed by the station must be provided with an accuracy ensuring that the errors on the estimate of the source energy are smaller than 20%.	
ILN-REQ-0.4	ILN-REQ-1.4	Source radiation = X°	The orientation of the instruments must be provided with a precision ensuring that the errors on the estimate of the source radiation are smaller than 10°.	
ILN-REQ-0.5	ILN-REQ-1.5	Data archiving and documentation	Data content, documentation, storage and archiving must ensure that an international community of researchers are able to understand these data and to implement research activities.	

Fig. 14 (*Continued*)

		INSTRUMENT REQUIREMENTS	
ILN-REQ-1.1; ILN-REQ-1.2	ILN-REQ-2.1	Time Stamp/Time Accuracy and Precision	Accuracy on the dating of the samples must be better than one tenth of the average sampling rate of the data channel. The aim is to use the data from various stations for network analysis.
ILN-REQ-1.1; ILN-REQ-1.2	ILN-REQ-2.2	Time Reference	Data samples must be provided in Coordinated Universal Time (UTC Time).
ILN-REQ-1.5	ILN-REQ-2.3	Sampling Rate	For a given data channel, data acquisition should be designed to be performed at constant sampling rate in the time reference of the instrument.
ILN-REQ-1.5	ILN-REQ-2.4	Format	Data and metadata must be provided in a format prescribed by the International Federation of Digital Seismograph Networks (FDSN) for the exchange of seismic data.
ILN-REQ-1.6	ILN-REQ-2.5	Units	Data must be provided in units of the international reference system (SI units).
ILN-REQ-1.3; ILN-REQ-1.5	ILN-REQ-2.6	Calibration Information	The amplitude of the instrument response must be provided with an accuracy better than 10% over the bandpass of the instrument during the entire lifetime of the instrument.
ILN-REQ-1.3; ILN-REQ-1.5	ILN-REQ-2.7	Calibration Information	The phase of the instrument response must be provided with an accuracy better than 10° over the bandpass of the instrument during the entire lifetime of the instrument.
ILN-REQ-1.5	ILN-REQ-2.8	Metadata and processing	Metadata must contain a description of all the processing steps from the physical unit to the digital (count) output of all data channels.

Fig. 14 (*Continued*)

INSTRUMENT REQUIREMENTS continued

ILN-REQ-1.3; ILN-REQ-1.5	ILN-REQ-2.9	Compression/ Decompression	If lossy compression is applied, it should allow signal reconstruction with an accuracy better than 10% of the signal energy.	
ILN-REQ-1.3; ILN-REQ-1.5	ILN-REQ-2.10	Aliasing	The instrument must be designed so that less than 0.1% of the signal above the Nyquist frequency is aliased in the bandpass of the instrument.	
ILN-REQ-1.5	ILN-REQ-2.11	Noise Estimates	Sensor and instrument noise must be estimated over the bandpass of the instrument and provided for each seismic channel in $m/s^2/\sqrt{(Hz)}$.	
ILN-REQ-1.5	ILN-REQ-2.12	Archiving	Data and metadata for all the instrument channels must be archived both in planetary databases and in geophysical sensor databases.	
ILN-REQ-1.5	ILN-REQ-2.13	Naming	A network code and a station code must be assigned to the geophysical station by the International Federation of Digital Seismograph Networks (FDSN).	
ILN-REQ-1.2; ILN-REQ-1.5	ILN-REQ-2.14	Station Location	The station location must be provided in a standard reference system defined by the International Astronomical Union (IAU).	
ILN-REQ-1.2	ILN-REQ-2.15	Station Location	The station location coordinates must be provided with an accuracy better than 25 m.	Half a wavelength, assuming highest frequency is 10 Hz and lowest S-wave velocity is 500 m/s.
ILN-REQ-1.4	ILN-REQ-2.16	Axis Orientation	The sensing direction of the instrument data channels must be provided with an accuracy better than 10°.	
ILN-REQ-1.5	ILN-REQ-2.17	Operations	Mission, platform and instrument operation activities impacting the signals above instrument noise level must be time-stamped, recorded and archived in the metadata for the instrument.	

ILN - International Lunar Network

Fig. 14 (*Continued*)

events (Nakamura et al. ([1981](#)) and updated in Oct. 2008). Section S5 contains attenuation parameters from Gillet et al. ([2017](#)). Section S6 contains a pdf version of the Minimum Requirements for an International Lunar Network (Fig. [14](#)). Section S7 contains a Jupyter Notebook to plot the transfer functions and the logarithmic compression parameters. Section S8 reproduces block diagrams for the mid- and short-period seismometers. Section S9 contains a table of the artificial impacts. Section S10 summarizes the current data availability. Section 11 contains the response files for the mid- and short-period seismometers.

Publisher's Note   Springer Nature remains neutral with regard to jurisdictional claims in published maps and institutional affiliations.

References

K. Aki, B. Chouet, Origin of coda waves, sources and attenuation. J. Geophys. Res. **80**, 3322–3342 (1975)

D. Anache-Ménier, B.A. van Tiggelen, L. Margerin, Phase statistics of seismic coda waves. Phys. Rev. Lett. **102**(24), 248501 (2009). https://doi.org/10.1103/PhysRevLett.102.248501

APL, We're Going to Titan, https://dragonfly.jhuapl.edu/ (2019). Accessed 2019-12-02

W.B. Banerdt, S.E. Smrekar, D. Banfield, D. Giardini, M. Golombek, C.L. Johnson, P. Lognonné, A. Spiga, T. Spohn, C. Perrin, S.C. Stähler, D. Antonangeli, S. Asmar, C. Beghein, N. Bowles, E. Bozdag, P. Chi, U. Christensen, J. Clinton, G.S. Collins, I. Daubar, V. Dehant, M. Drilleau, M. Fillingim, W. Folkner, R.F. Garcia, J. Garvin, J. Grant, M. Grott, J. Grygorczuk, T. Hudson, J.C.E. Irving, G. Kargl, T. Kawamura, S. Kedar, S. King, B. Knapmeyer-Endrun, M. Knapmeyer, M. Lemmon, R. Lorenz, J.N. Maki, L. Margerin, S.M. McLennan, C. Michaut, D. Mimoun, A. Mittelholz, A. Mocquet, P. Morgan, N.T. Mueller, N. Murdoch, S. Nagihara, C. Newman, F. Nimmo, M. Panning, W.T. Pike, A.-C. Plesa, S. Rodriguez, J.A. Rodriguez-Manfredi, C.T. Russell, N. Schmerr, M. Siegler, S. Stanley, E. Stutzmann, N. Teanby, J. Tromp, M. van Driel, N. Warner, R. Weber, M. Wieczorek, Initial results from the InSight mission on Mars. Nat. Geosci. **13**(3), 183–189 (2020). https://doi.org/10.1038/s41561-020-0544-y

J.R. Bates, W.W. Lauderdale, H. Kernaghan, ALSEP Termination Report (NASA Reference Publication 1036, 1979). Last accessed 2018-11-13. https://ntrs.nasa.gov/search.jsp?R=19790014808

J.-F. Blanchette-Guertin, C.L. Johnson, J.F. Lawrence, Investigation of scattering in lunar seismic coda. J. Geophys. Res., Planets **117**, E06003 (2012). https://doi.org/10.1029/2011JE004042

M. Brzostowski, A. Brzostowski, Archiving the Apollo active seismic data. Lead. Edge **28**(4), 414–416 (2009). https://doi.org/10.1190/1.3112756

R.C. Bulow, C.L. Johnson, P.M. Shearer, New events discovered in the Apollo lunar seismic data. J. Geophys. Res. **110**, E10003 (2005). https://doi.org/10.1029/2005JE002414

R.C. Bulow, C.L. Johnson, B.G. Bills, P.M. Shearer, Temporal and spatial properties of some deep moonquake clusters. J. Geophys. Res. **112**, E09003 (2007). https://doi.org/10.1029/2006JE002847

C.H. Cheng, M.N. Toksöz, Tidal stresses in the Moon. J. Geophys. Res. **83**(B2), 845 (1978). https://doi.org/10.1029/JB083iB02p00845

A.M. Dainty, M.N. Toksöz, Seismic codas on the Earth and the Moon: a comparison. Phys. Earth Planet. Inter. **26**(4), 250–260 (1981). https://doi.org/10.1016/0031-9201(81)90029-7

A.M. Dainty, M.N. Toksöz, K.R. Anderson, P.J. Pines, Y. Nakamura, G. Latham, Seismic scattering and shallow structure of the Moon in Oceanus Procellarum. Moon **9**, 11–29 (1974). https://doi.org/10.1007/BF00565388

I. Daubar, P. Lognonné, N.A. Teanby, K. Miljkovic, J. Stevanović, J. Vaubaillon, B. Kenda, T. Kawamura, J. Clinton, A. Lucas, M. Drilleau, C. Yana, G.S. Collins, D. Banfield, M. Golombek, S. Kedar, N. Schmerr, R. Garcia, S. Rodriguez, T. Gudkova, S. May, M. Banks, J. Maki, E. Sansom, F. Karakostas, M. Panning, N. Fuji, J. Wookey, M. van Driel, M. Lemmon, V. Ansan, M. Böse, S. Stähler, H. Kanamori, J. Richardson, S. Smrekar, W.B. Banerdt, Impact-seismic investigations of the InSight mission. Space Sci. Rev. **214**(8), 132 (2018). https://doi.org/10.1007/s11214-018-0562-x

D.N. DellaGiustina, S.H. Bailey, V.J. Bray, P. Dahl, N.C. Schmerr, B. Avenson, A.G. Marusiak, E.C. Pettit, On-lander seismology at an ocean worlds analog site in Northwest Greenland, in *Lunar and Planetary Science Conference*. Lunar and Planetary Science Conference (2019), p. 2764

J.-L. Dimech, B. Knapmeyer-Endrun, D. Phillips, R.C. Weber, Preliminary analysis of newly recovered Apollo 17 seismic data. Results Phys. **7**, 4457–4458 (2017). https://doi.org/10.1016/j.rinp.2017.11.029

F. Duennebier, G.H. Sutton, Thermal moonquakes. J. Geophys. Res. **79**(29), 4351–4363 (1974). https://doi.org/10.1029/JB079i029p04351

C. Frohlich, Y. Nakamura, The physical mechanisms of deep moonquakes and intermediate-depth earthquakes: how similar and how different? Phys. Earth Planet. Inter. **173**(3–4), 365–374 (2009). https://doi.org/10.1016/j.pepi.2009.02.004

J. Gagnepain-Beyneix, P. Lognonné, H. Chenet, D. Lombardi, T. Spohn, A seismic model of the lunar mantle and constraints on temperature and mineralogy. Phys. Earth Planet. Inter. **159**(3–4), 140–166 (2006). https://doi.org/10.1016/j.pepi.2006.05.009

R.F. Garcia, J. Gagnepain-Beyneix, S. Chevrot, P. Lognonné, Very preliminary reference Moon model. Phys. Earth Planet. Inter. **188**, 96–113 (2011). https://doi.org/10.1016/j.pepi.2011.06.015

R.F. Garcia, A. Khan, M. Drilleau, L. Margerin, T. Kawamura, D. Sun, M.A. Wieczorek, A. Rivoldini, C. Nunn, R.C. Weber, A.G. Marusiak, P. Lognonné, Y. Nakamura, P. Zhu, Lunar seismology: an update on interior structure models. Space Sci. Rev. **215**, 50 (2019). https://doi.org/10.1007/s11214-019-0613-y

D. Giardini, P. Lognonné, W.B. Banerdt, W.T. Pike, U. Christensen, S. Ceylan, J.F. Clinton, M. van Driel, S.C. Stähler, M. Böse, R.F. Garcia, A. Khan, M. Panning, C. Perrin, D. Banfield, E. Beucler, C. Charalambous, F. Euchner, A. Horleston, A. Jacob, T. Kawamura, S. Kedar, G. Mainsant, J.-R. Scholz, S.E. Smrekar, A. Spiga, C. Agard, D. Antonangeli, S. Barkaoui, E. Barrett, P. Combes, V. Conejero, I. Daubar, M. Drilleau, C. Ferrier, T. Gabsi, T. Gudkova, K. Hurst, F. Karakostas, S. King, M. Knapmeyer, B. Knapmeyer-Endrun, R. Llorca-Cejudo, A. Lucas, L. Luno, L. Margerin, J.B. McClean, D. Mimoun, N. Murdoch, F. Nimmo, M. Nonon, C. Pardo, A. Rivoldini, J.A.R. Manfredi, H. Samuel, M. Schimmel, A.E. Stott, E. Stutzmann, N. Teanby, T. Warren, R.C. Weber, M. Wieczorek, C. Yana, The seismicity of Mars. Nat. Geosci. **13**(3), 205–212 (2020). https://doi.org/10.1038/s41561-020-0539-8

J.J. Giganti, J.V. Larson, J.P. Richard, R.L. Tobias, J. Weber, Lunar surface gravimeter experiment—final report. Technical report. University of Maryland, United States (1977)

K. Gillet, L. Margerin, M. Calvet, M. Monnereau, Scattering attenuation profile of the Moon: implications for shallow moonquakes and the structure of the megaregolith. Phys. Earth Planet. Inter. **262**, 28–40 (2017). https://doi.org/10.1016/j.pepi.2016.11.001

D. Goh, China's Chang'e 5 Lunar Mission Delayed to 2019, Chang'e 4 on Schedule, http://www.spacetechasia.com/chinas-change-5-lunar-mission-delayed-to-2019-change-4-on-schedule/ (2018). Accessed 2018-07-24

N.R. Goins, Lunar seismology: the internal structure of the Moon. PhD thesis, M.I.T. (1978). Last accessed 2018-11-13. https://ntrs.nasa.gov/search.jsp?R=19790009611

J.W. Goodman, *Statistical Optics*, 2nd edn. (John Wiley & Sons Inc., Hoboken, 2015). 978-1-119-00945-0

T.V. Gudkova, P. Lognonne, J. Gagnepain-Beyneix, Large impacts detected by the Apollo seismometers: impactor mass and source cutoff frequency estimations. Icarus **211**(2), 1049–1065 (2011). https://doi.org/10.1016/j.icarus.2010.10.028

I. Haase, P. Gläser, M. Knapmeyer, J. Oberst, M.S. Robinson, Improved coordinates of the Apollo 17 Lunar Seismic Profiling Experiment (LSPE) components, in *44th Lunar Planet. Sci. Conf.* (2013). Abstract #1966

A. Heffels, M. Knapmeyer, J. Oberst, I. Haase, Re-evaluation of Apollo 17 lunar seismic profiling experiment data. Planet. Space Sci. **135**, 43–54 (2017). https://doi.org/10.1016/j.pss.2016.11.007

P. Horvath, Analysis of lunar seismic signals: determination of instrumental parameters and seismic velocity distributions. PhD thesis, University of Texas at Dallas (1979)

JAXA, Smart Lander for Investigating Moon (SLIM), http://global.jaxa.jp/projects/sas/slim/ (2018). Accessed 2019-10-01

T. Kawamura, N. Kobayashi, S. Tanaka, L. Lognonné, Lunar surface gravimeter as a lunar seismometer: investigation of a new source of seismic information on the Moon. J. Geophys. Res., Planets **120**, 343–358 (2015). https://doi.org/10.1002/2014JE004724

T. Kawamura, P. Lognonné, Y. Nishikawa, S. Tanaka, Evaluation of deep moonquake source parameters: implication for fault characteristics and thermal state. J. Geophys. Res., Planets **122**(7), 1487–1504 (2017). https://doi.org/10.1002/2016JE005147

A. Khan, K. Mosegaard, K.L. Rasmussen, A new seismic velocity model for the Moon from a Monte Carlo inversion of the Apollo lunar seismic data. Geophys. Res. Lett. **27**(11), 1591–1594 (2000). https://doi.org/10.1029/1999GL008452

B. Knapmeyer-Endrun, C. Hammer, Identification of new events in Apollo 16 lunar seismic data by Hidden Markov Model-based event detection and classification. J. Geophys. Res., Planets **120**(10), 1620–1645 (2015). https://doi.org/10.1002/2015JE004862

R.L. Kovach, J.S. Watkins, T. Landers, Active seismic experiment, in *Apollo 14—Preliminary Science Report, NASA SP-272* (1971). Last accessed 2018-11-13. https://ntrs.nasa.gov/search.jsp?R=19710021477

R.L. Kovach, J.S. Watkins, P. Talwani, Active seismic experiment, in *Apollo 16—Preliminary Science Report, NASA SP-315* (1972). Last accessed 2018-11-13. https://ntrs.nasa.gov/search.jsp?R=19730013002

R.L. Kovach, J.S. Watkins, P. Talwani, Lunar seismic profiling experiment, in *Apollo 17—Preliminary Science Report, NASA SP-330* (1973). Last accessed 2018-11-13. https://ntrs.nasa.gov/search.jsp?R=19740010315

D.R. Lammlein, Lunar seismicity and tectonics. Phys. Earth Planet. Inter. **14**, 224–273 (1977). https://doi.org/10.1016/0031-9201(77)90175-3

D.R. Lammlein, G.V. Latham, J. Dorman, Y. Nakamura, M. Ewing, Lunar seismicity, structure, and tectonics. Rev. Geophys. **12**(1), 1–21 (1974). https://doi.org/10.1029/RG012i001p00001

G.V. Latham, M. Ewing, F. Press, G. Sutton, J. Dorman, Y. Nakamura, N. Toksoz, F. Duennebier, D. Lammlein, Passive seismic experiment, in *Apollo 14: Preliminary Science Report, NASA SP-272* (1971)

W.W. Lauderdale, W.F. Eichelman, Passive seismic experiment (NASA Experiment S-031), in *Apollo Scientific Experiments Data Handbook, NASA TM-X-58131* (1974)

P. Lognonné, C.L. Johnson, Planetary seismology, in *Treatise on Geophysics*, ed. by G. Schubert (Elsevier, Oxford, 2015), pp. 65–120. 978-0-444-53803-1. https://doi.org/10.1016/B978-0-444-53802-4.00167-6

P. Lognonné, T. Kawamura, Impact seismology on terrestrial and giant planets, in *Extraterrestrial Seismology*, ed. by V.C.H. Tong, R.A. Garcia (Cambridge University Press, Cambridge, 2015), pp. 250–263. 978-1-107-30066-8. https://doi.org/10.1017/CBO9781107300668.021

P. Lognonné, J. Gagnepain-Beyneix, H. Chenet, A new seismic model of the Moon: implications for structure, thermal evolution and formation of the Moon. Earth Planet. Sci. Lett. **211**(1–2), 27–44 (2003). https://doi.org/10.1016/S0012-821X(03)00172-9

P. Lognonné, W.B. Banerdt, D. Giardini, W.T. Pike, U. Christensen, P. Laudet, S. de Raucourt, P. Zweifel, S. Calcutt, M. Bierwirth, K.J. Hurst, F. Ijpelaan, J.W. Umland, R. Llorca-Cejudo, S.A. Larson, R.F. Garcia, S. Kedar, B. Knapmeyer-Endrun, D. Mimoun, A. Mocquet, M.P. Panning, R.C. Weber, A. Sylvestre-Baron, G. Pont, N. Verdier, L. Kerjean, L.J. Facto, V. Gharakanian, J.E. Feldman, T.L. Hoffman, D.B. Klein, K. Klein, N.P. Onufer, J. Paredes-Garcia, M.P. Petkov, J.R. Willis, S.E. Smrekar, M. Drilleau, T. Gabsi, T. Nebut, O. Robert, S. Tillier, C. Moreau, M. Parise, G. Aveni, S. Ben Charef, Y. Bennour, T. Camus, P.A. Dandonneau, C. Desfoux, B. Lecomte, O. Pot, P. Revuz, D. Mance, J. ten Pierick, N.E. Bowles, C. Charalambous, A.K. Delahunty, J. Hurley, R. Irshad, H. Liu, A.G. Mukherjee, I.M. Standley, A.E. Stott, J. Temple, T. Warren, M. Eberhardt, A. Kramer, W. Kühne, E.-P. Miettinen, M. Monecke, C. Aicardi, M. André, J. Baroukh, A. Borrien, A. Bouisset, P. Boutte, K. Brethomé, C. Brysbaert, T. Carlier, M. Deleuze, J.M. Desmarres, D. Dilhan, C. Doucet, D. Faye, N. Faye-Refalo, R. Gonzalez, C. Imbert, C. Larigauderie, E. Locatelli, L. Luno, J.-R. Meyer, F. Mialhe, J.M. Mouret, M. Nonon, Y. Pahn, A. Paillet, P. Pasquier, G. Perez, R. Perez, L. Perrin, B. Pouilloux, A. Rosak, I. Savin de Larclause, J. Sicre, M. Sodki, N. Toulemont, B. Vella, C. Yana, F. Alibay, O.M. Avalos, M.A. Balzer, P. Bhandari, E. Blanco, B.D. Bone, J.C. Bousman, P. Bruneau, F.J. Calef, R.J. Calvet, S.A. D'Agostino, G. de los Santos, R.G. Deen, R.W. Denise, J. Ervin, N.W. Ferraro, H.E. Gengl, F. Grinblat, D. Hernandez, M. Hetzel, M.E. Johnson, L. Khachikyan, J.Y. Lin, S.M. Madzunkov, S.L. Marshall, I.G. Mikellides, E.A. Miller, W. Raff, J.E. Singer, C.M. Sunday, J.F. Villalvazo, M.C. Wallace, D. Banfield, J.A. Rodriguez-Manfredi, C.T. Russell, A. Trebi-Ollennu, J.N. Maki, E. Beucler, M. Böse, C. Bonjour, J.L. Berenguer, S. Ceylan, J. Clinton, V. Conejero, I. Daubar, V. Dehant, P. Delage, F. Euchner, I. Estève, L. Fayon, L. Ferraioli, C.L. Johnson, J. Gagnepain-Beyneix, M. Golombek, A. Khan, T. Kawamura, B. Kenda, P. Labrot, N. Murdoch, C. Pardo, C. Perrin, L. Pou, A. Sauron, D. Savoie, S. Stähler, E. Stutzmann, N.A. Teanby, J. Tromp, M. van Driel, M. Wieczorek, R. Widmer-Schnidrig, J. Wookey, SEIS: insight's seismic experiment for internal structure of Mars. Space Sci. Rev. **215**(1), 12 (2019). https://doi.org/10.1007/s11214-018-0574-6

P. Lognonné, W.B. Banerdt, W.T. Pike, D. Giardini, U. Christensen, R.F. Garcia, T. Kawamura, S. Kedar, B. Knapmeyer-Endrun, L. Margerin, F. Nimmo, M. Panning, B. Tauzin, J.-R. Scholz, D. Antonangeli, S. Barkaoui, E. Beucler, F. Bissig, N. Brinkman, M. Calvet, S. Ceylan, C. Charalambous, P. Davis, M. van Driel, M. Drilleau, L. Fayon, R. Joshi, B. Kenda, A. Khan, M. Knapmeyer, V. Lekic, J. McClean, D. Mimoun, N. Murdoch, L. Pan, C. Perrin, B. Pinot, L. Pou, S. Menina, S. Rodriguez, C. Schmelzbach, N. Schmerr, D. Sollberger, A. Spiga, S. Stähler, A. Stott, E. Stutzmann, S. Tharimena, R. Widmer-Schnidrig, F. Andersson, V. Ansan, C. Beghein, M. Böse, E. Bozdag, J. Clinton, I. Daubar, P. Delage, N. Fuji, M. Golombek, M. Grott, A. Horleston, K. Hurst, J. Irving, A. Jacob, J. Knollenberg, S. Krasner, C. Krause, R. Lorenz, C. Michaut, R. Myhill, T. Nissen-Meyer, J. ten Pierick, A.-C. Plesa, C. Quantin-Nataf, J. Robertsson, L. Rochas, M. Schimmel, S. Smrekar, T. Spohn, N. Teanby, J. Tromp, J. Vallade, N. Verdier, C. Vrettos, R. Weber, D. Banfield, E. Barrett, M. Bierwirth, S. Calcutt, N. Compaire, C.L. Johnson, D. Mance, F. Euchner, L. Kerjean, G. Mainsant, A. Mocquet, J.A. Rodriguez Manfredi, G. Pont, P. Laudet, T. Nebut, S. de Raucourt, O. Robert, C.T. Russell, A. Sylvestre-Baron, S. Tillier, T. Warren, M. Wieczorek, C. Yana, P. Zweifel, Constraints on the shallow elastic and anelastic structure of Mars from InSight seismic data. Nat. Geosci. **13**(3), 213–220 (2020). https://doi.org/10.1038/s41561-020-0536-y

LROC, LROC—Featured Lunar Sites, http://www.lroc.asu.edu/featured_sites/ (2017). Accessed 2018-08-02

A.G. Marusiak, N.C. Schmerr, D. DellaGiustina, H. Bailey, V.J. Bray, J.I. Brodbeck, N. Habib, E.C. Pettit, C.G. Carr, N. Wagner, R.C. Weber, P. Dahl, B. Avenson, The Seismometer to Investigate Ice and Ocean Structure (SIIOS) in Greenland: testing instrument performance on an icy world analog, in *AGU Fall Meeting Abstracts* (2018)

A.G. Marusiak, N.C. Schmerr, D.N. DellaGiustina, E.C. Pettit, P.H. Dahl, B. Avenson, S.H. Bailey, V.J. Bray, N. Wagner, C.G. Carr, R.C. Weber, The deployment of the Seismometer to Investigate Ice and Ocean Structure (SIIOS) on Gulkana Glacier, Alaska. Seismol. Res. Lett. (2020). https://doi.org/10.1785/0220190328

B. McAllister, J. Kerr, J. Zimmer, R. Kovach, J. Watkins, A seismic refraction system for lunar use. IEEE Trans. Geosci. Electron. **7**(3), 164–171 (1969). https://doi.org/10.1109/TGE.1969.271374

J.R. McDowell, The active seismic experiment, in *Apollo 14 and 16 Active Seismic Experiments and Apollo 17 Lunar Seismic Profiling—Final Report*, ed. by R.L. Kovach, J.S. Watkins (Stanford University, United States, 1976). Last accessed 2018-10-18. https://ntrs.nasa.gov/search.jsp?R=19760018052

A. McGarr, G.V. Latham, D.E. Gault, Meteoroid impacts as sources of seismicity on the Moon. J. Geophys. Res. **74**, 5981–5994 (1969). https://doi.org/10.1029/JB074i025p05981

D. Mimoun, M.A. Wieczorek, L. Alkalai, W.B. Banerdt, D. Baratoux, J.-L. Bougeret, S. Bouley, B. Cecconi, H. Falcke, J. Flohrer, R.F. Garcia, R. Grimm, M. Grott, L. Gurvits, R. Jaumann, C.L. Johnson, M. Knapmeyer, N. Kobayashi, A. Konovalenko, D. Lawrence, M.L. Feuvre, P. Lognonné, C. Neal, J. Oberst, N. Olsen, H. Röttgering, T. Spohn, S. Vennerstrom, G. Woan, P. Zarka, Farside explorer: unique science from a mission to the farside of the Moon. Exp. Astron. **33**(2–3), 529–585 (2012). https://doi.org/10.1007/s10686-011-9252-3

MSC, MSC internal note: data processing plan for Apollo lunar surface and subsatellite experiments (NASA, 1971). MSC-04434

S. Nagihara, Y. Nakamura, D.R. Williams, P.T. Taylor, S.A. McLaughlin, H.K. Hills, W.S. Kiefer, R.C. Weber, J.-L. Dimech, D. Phillips, C. Nunn, G.K. Schmidt, Recent achievement by the SSERVI ALSEP data recovery focus group, in *2017 Annual Meeting of the Lunar Exploration Analysis Group (LEAG)* (2017). Abstract #5017

S. Nagihara, W.S. Kiefer, P.T. Taylor, D.R. Williams, Y. Nakamura, Examination of the long-term subsurface warming observed at the Apollo 15 and 17 sites utilizing the newly restored heat flow experiment data from 1975 to 1977. J. Geophys. Res., Planets **123**(5), 1125–1139 (2018). https://doi.org/10.1029/2018JE005579

Y. Nakamura, HFT events: shallow moonquakes? Phys. Earth Planet. Inter. **14**(3), 217–223 (1977). https://doi.org/10.1016/0031-9201(77)90174-1

Y. Nakamura, A1 moonquakes—source distribution and mechanism. Proc. Lunar Planet. Sci. Conf. 9th, 3589–3607 (1978)

Y. Nakamura, Shallow moonquakes—how they compare with earthquakes. Proc. Lunar Planet. Sci. Conf. 11th, 1847–1853 (1980)

Y. Nakamura, Seismic velocity structure of the lunar mantle. J. Geophys. Res. **88**, 677–686 (1983). https://doi.org/10.1029/JB088iB01p00677

Y. Nakamura, New identification of deep moonquakes in the Apollo lunar seismic data. Phys. Earth Planet. Inter. **139**(3–4), 197–205 (2003). https://doi.org/10.1016/j.pepi.2003.07.017

Y. Nakamura, Farside deep moonquakes and deep interior of the Moon. J. Geophys. Res. **110**, E01001 (2005). https://doi.org/10.1029/2004JE002332

Y. Nakamura, Timing problem with the Lunar Module impact data as recorded by the LSPE and corrected near-surface structure at the Apollo 17 landing site. J. Geophys. Res. **116**, E12005 (2011). https://doi.org/10.1029/2011JE003972

Y. Nakamura, G.V. Latham, H.J. Dorman, A.B.K. Ibrahim, J. Koyama, P. Horvath, Shallow moonquakes—depth, distribution and implications as to the present state of the lunar interior. Proc. Lunar Planet. Sci. Conf. 10th **3** (1979)

Y. Nakamura, G.V. Latham, H.J. Dorman, Apollo lunar seismic experiment—final summary. J. Geophys. Res., Solid Earth **87**(S01), A117–A123 (1982). https://doi.org/10.1029/JB087iS01p0A117

Y. Nakamura, G.V. Latham, H.J. Dorman, J.E. Harris, Passive seismic experiment long-period event catalog, final version (Galveston Geophysics Laboratory of the University of Texas at Austin, Marine Science Institute, 1981). UTIG Technical Report No. 18

National Research Council, *Vision and Voyages for Planetary Science in the Decade 2013–2022* (National Academies Press, Washington, D.C., 2011). 978-0-309-22464-2. https://doi.org/10.17226/13117

C. Nunn, Y. Nakamura, H. Igel, Apollo passive seismic experiments: lunar data in SEED format. AGU Fall Meeting, New Orleans, 2017 (2017)

J. Oberst, Unusually high stress drops associated with shallow moonquakes. J. Geophys. Res. **92**(B2), 1397–1405 (1987). https://doi.org/10.1029/JB092iB02p01397

J. Oberst, Y. Nakamura, A search for clustering among the meteoroid impacts detected by the Apollo lunar seismic network. Icarus **91**(2), 315–325 (1991). https://doi.org/10.1016/0019-1035(91)90027-Q

J.B. Plescia, M.S. Robinson, R. Wagner, R. Baldridge, Ranger and Apollo S-IVB spacecraft impact craters. Planet. Space Sci. **124**, 15–35 (2016). https://doi.org/10.1016/j.pss.2016.01.002

A.E. Saal, E.H. Hauri, M.L. Cascio, J.A. Van Orman, M.C. Rutherford, R.F. Cooper, Volatile content of lunar volcanic glasses and the presence of water in the Moon's interior. Nature **454**(7201), 192–195 (2008). https://doi.org/10.1038/nature07047

H. Sato, M.C. Fehler, T. Maeda, *Seismic Wave Propagation and Scattering in the Heterogeneous Earth*, 2nd edn. (Springer Berlin Heidelberg, Berlin, Heidelberg, 2012). 978-3-642-23029-5. https://doi.org/10.1007/978-3-642-23029-5

C. Shearer, G. Tahu, Lunar Geophysical Network (LGN) (NASA, 2011). Accessed 2018-07-24. https://archive.org/details/LunarGeophysicalNetworklgn

S. Stein, M. Wysession, *An Introduction to Seismology, Earthquakes, and Earth Structure* (Blackwell Pub., Malden, 2003). 978-0-86542-078-6

P.J. Stooke, Spacecraft impacts on the Moon: Chang'e 1, Apollo LM ascent stages. 48th Lunar Planet. Sci. Conf. (2017). Abstract #1031

G.H. Sutton, G.V. Latham, Analysis of a feedback-controlled seismometer. J. Geophys. Res. **69**(18), 3865–3882 (1964). https://doi.org/10.1029/JZ069i018p03865

N.A. Teanby, J. Wookey, Seismic detection of meteorite impacts on Mars. Phys. Earth Planet. Inter. **186**(1–2), 70–80 (2011). https://doi.org/10.1016/j.pepi.2011.03.004

Teledyne, Final technical report for ALSEP passive seismic experiment subsystem program. Report No. 640-0768-0057. Subcontract SC-0200 (1968)

S.D. Vance, S. Kedar, M.P. Panning, S.C. Stähler, B.G. Bills, R.D. Lorenz, H.-H. Huang, W.T. Pike, J.C. Castillo, P. Lognonné, V.C. Tsai, A.R. Rhoden, Vital signs: seismology of icy ocean worlds. Astrobiology **18**(1), 37–53 (2018). https://doi.org/10.1089/ast.2016.1612

R.V. Wagner, D.M. Nelson, J.B. Plescia, M.S. Robinson, E.J. Speyerer, E. Mazarico, Coordinates of anthropogenic features on the Moon. Icarus **283**(Supplement C), 92–103 (2017). https://doi.org/10.1016/j.icarus.2016.05.011

J. Weber, J.V. Larson, Lunar surface gravimeter experiment. Technical report, Physics Department, University of Maryland, United States, n.d.

R.C. Weber, P. Lin, E.J. Garnero, Q. Williams, P. Lognonné, Seismic detection of the lunar core. Science **331**, 309–312 (2011). https://doi.org/10.1126/science.1199375

J.G. Williams, D.H. Boggs, W.M. Folkner, DE421 lunar orbit, physical librations, and surface coordinates (Jet Propulsion Lab., Calif. Inst. of Tech., Pasadena, CA, 2008). JPL Mem. IOM 335-JW, DB, WF-20080314-001

R. Yamada, The Apollo seismometer responses, http://www.darts.isas.jaxa.jp/planet/seismology/apollo/The_Apollo_Seismometer_Responses.pdf (2012). Last accessed 2017-11-29

R. Yamada, R.F. Garcia, P. Lognonné, M.L. Feuvre, M. Calvet, J. Gagnepain-Beyneix, Optimisation of seismic network design: application to a geophysical international lunar network. Planet. Space Sci. **59**(4), 343–354 (2011). https://doi.org/10.1016/j.pss.2010.12.007

M. Yasui, E. Matsumoto, M. Arakawa, Experimental study on impact-induced seismic wave propagation through granular materials. Icarus **260**, 320–331 (2015). https://doi.org/10.1016/j.icarus.2015.07.032

N. Zhao, P. Zhu, B. Zhang, Y. Yuan, Moonquake relocation. Earth Sci., J. China Univ. Geosci. **40**(7), 1276 (2015). In Chinese. https://doi.org/10.3799/dqkx.2015.107

Terms and Conditions

Springer Nature journal content, brought to you courtesy of Springer Nature Customer Service Center GmbH ("Springer Nature").

Springer Nature supports a reasonable amount of sharing of research papers by authors, subscribers and authorised users ("Users"), for small-scale personal, non-commercial use provided that all copyright, trade and service marks and other proprietary notices are maintained. By accessing, sharing, receiving or otherwise using the Springer Nature journal content you agree to these terms of use ("Terms"). For these purposes, Springer Nature considers academic use (by researchers and students) to be non-commercial.

These Terms are supplementary and will apply in addition to any applicable website terms and conditions, a relevant site licence or a personal subscription. These Terms will prevail over any conflict or ambiguity with regards to the relevant terms, a site licence or a personal subscription (to the extent of the conflict or ambiguity only). For Creative Commons-licensed articles, the terms of the Creative Commons license used will apply.

We collect and use personal data to provide access to the Springer Nature journal content. We may also use these personal data internally within ResearchGate and Springer Nature and as agreed share it, in an anonymised way, for purposes of tracking, analysis and reporting. We will not otherwise disclose your personal data outside the ResearchGate or the Springer Nature group of companies unless we have your permission as detailed in the Privacy Policy.

While Users may use the Springer Nature journal content for small scale, personal non-commercial use, it is important to note that Users may not:

1. use such content for the purpose of providing other users with access on a regular or large scale basis or as a means to circumvent access control;

2. use such content where to do so would be considered a criminal or statutory offence in any jurisdiction, or gives rise to civil liability, or is otherwise unlawful;

3. falsely or misleadingly imply or suggest endorsement, approval , sponsorship, or association unless explicitly agreed to by Springer Nature in writing;

4. use bots or other automated methods to access the content or redirect messages

5. override any security feature or exclusionary protocol; or

6. share the content in order to create substitute for Springer Nature products or services or a systematic database of Springer Nature journal content.

In line with the restriction against commercial use, Springer Nature does not permit the creation of a product or service that creates revenue, royalties, rent or income from our content or its inclusion as part of a paid for service or for other commercial gain. Springer Nature journal content cannot be used for inter-library loans and librarians may not upload Springer Nature journal content on a large scale into their, or any other, institutional repository.

These terms of use are reviewed regularly and may be amended at any time. Springer Nature is not obligated to publish any information or content on this website and may remove it or features or functionality at our sole discretion, at any time with or without notice. Springer Nature may revoke this licence to you at any time and remove access to any copies of the Springer Nature journal content which have been saved.

To the fullest extent permitted by law, Springer Nature makes no warranties, representations or guarantees to Users, either express or implied with respect to the Springer nature journal content and all parties disclaim and waive any implied warranties or warranties imposed by law, including merchantability or fitness for any particular purpose.

Please note that these rights do not automatically extend to content, data or other material published by Springer Nature that may be licensed from third parties.

If you would like to use or distribute our Springer Nature journal content to a wider audience or on a regular basis or in any other manner not expressly permitted by these Terms, please contact Springer Nature at

onlineservice@springernature.com